



1 **IAPv4 ocean temperature and ocean heat content gridded**  
2 **dataset**

3 Lijing Cheng<sup>1,11\*</sup>, Yuying Pan<sup>1,11</sup>, Zhetao Tan<sup>1,11</sup>, Huayi Zheng<sup>1,11</sup>, Yujing Zhu<sup>1,11</sup>, Wangxu  
4 Wei<sup>1,11</sup>, Juan Du<sup>1</sup>, Huifeng Yuan<sup>2,11</sup>, Guancheng Li<sup>3</sup>, Hanlin Ye<sup>1</sup>, Viktor Gouretski<sup>1</sup>,  
5 Yuanlong Li<sup>4,11</sup>, Kevin E. Trenberth<sup>5,6</sup>, John Abraham<sup>7</sup>, Yuchun Jin<sup>4,11</sup>, Franco Reseghetti<sup>8</sup>,  
6 Xiaopei Lin<sup>9</sup>, Bing Zhang<sup>4,11</sup>, Gengxin Chen<sup>10, 11</sup>, Michael E. Mann<sup>12</sup>, Jiang Zhu<sup>1,11</sup>

7  
8 <sup>1</sup> Institute of Atmospheric Physics, Chinese Academy of Sciences, Beijing, China, 100029.

9 <sup>2</sup> Computer Network Information Center, Chinese Academy of Sciences, Beijing, 100083.

10 <sup>3</sup> Eco-Environmental Monitoring and Research Center, Pearl River Valley and South China  
11 Sea Ecology and Environment Administration, Ministry of Ecology and Environment,  
12 PRC, Guangzhou 510611, China.

13 <sup>4</sup> Institute of Oceanography, Chinese Academy of Sciences, Qingdao, China.

14 <sup>5</sup> National Center for Atmospheric Research, PO Box 3000, Boulder, CO 80307, USA.

15 <sup>6</sup> University of Auckland, Auckland, New Zealand.

16 <sup>7</sup> University of St. Thomas, School of Engineering, 2115 Summit Ave., St Paul, MN  
17 55105, USA.

18 <sup>8</sup> Italian National Agency for New Technologies, Energy and Sustainable Economic  
19 Development, S. Teresa Research Center, Lerici 19032, Italy.

20 <sup>9</sup> Frontier Science Center for Deep Ocean Multispheres and Earth System and Physical  
21 Oceanography Laboratory, Ocean University of China, Qingdao, China.

22 <sup>10</sup> State Key Laboratory of Tropical Oceanography, South China Sea Institute of  
23 Oceanology, Chinese Academy of Sciences, Guangzhou, China

24 <sup>11</sup> University of Chinese Academy of Sciences, Beijing, China.

25 <sup>12</sup> Dept. of Earth and Environmental Science, University of Pennsylvania, Philadelphia PA,  
26 USA

27

28 *Correspondence to:* Lijing Cheng (chenglij@mail.iap.ac.cn)

29



30 **Abstract.** Ocean observational gridded products are vital for climate monitoring, ocean  
31 and climate research, model evaluation, and supporting climate mitigation and adaptation  
32 measures. This paper describes the 4<sup>th</sup> version of the Institute of Atmospheric Physics  
33 (IAPv4) ocean temperature and ocean heat content (OHC) objective analysis product. It  
34 accounts for recent developments in quality control (QC) procedures, climatology, bias  
35 correction, vertical and horizontal interpolation, and mapping and is available for the upper  
36 6000 m (119 levels) since 1940 (more reliable after ~1957) for monthly and  $1^\circ \times 1^\circ$   
37 temporal and spatial resolutions. The IAPv4 is compared with the previous version, IAPv3,  
38 and to the other data products, sea surface temperatures (SSTs), and satellite observations.  
39 It has a slightly stronger long-term upper 2000 m OHC increase than IAPv3 for 1955-  
40 2023, mainly because of newly developed bias corrections. IAPv4 OHC 0-2000 m trend is  
41 also higher during 2005-2023 than IAPv3. The first level of IAPv4 is consistent with  
42 independent SST datasets. The month-to-month OHC variability for IAPv4 is desirably  
43 less than IAPv3 and other OHC products investigated in this study; annual variations are  
44 consistent with the net energy imbalance at the top of the atmosphere, and the sea level  
45 budget can be closed within uncertainty. The gridded product is freely accessible at:  
46 <http://dx.doi.org/10.12157/IOCAS.20240117.002> for temperature data (Cheng et al.,  
47 [2024a](http://dx.doi.org/10.12157/IOCAS.20240117.001)) and <http://dx.doi.org/10.12157/IOCAS.20240117.001> for ocean heat content data  
48 (Cheng et al., 2024b).

49

## 50 1. Introduction

51 Observational gridded products are essential for understanding the ocean, the  
52 atmosphere, and climate change; they support policy decisions and social-economy  
53 developments (Abraham et al., 2022; Abraham and Cheng, 2022; Cheng et al., 2022a). For  
54 instance, many of the climate indicators used in the Working Group I report of the 6<sup>th</sup>  
55 Intergovernmental Panel on Climate Change (IPCC-AR6-WG1) are gridded products  
56 (Gulev et al., 2021; IPCC, 2021), mainly because the raw oceanic data suffer from  
57 inhomogeneous data quality and irregular and incomplete data coverage (Abraham et al.,  
58 2013; Cheng et al., 2022a; Meyssignac et al., 2019).



59 As more than 90% of the Earth's energy imbalance (EEI) in the past half-century has  
60 accumulated in the ocean, increasing ocean temperature ( $T$ ) and ocean heat content (OHC)  
61 are essential climate variables for monitoring, understanding, and projecting climate  
62 change (Hansen et al., 2011; Trenberth, 2022; Trenberth et al., 2009; von Schuckmann et  
63 al., 2020). OHC also impacts air-sea and ice-sea interactions and thus exerts a considerable  
64 influence over the other components of the climate system. It provides critical feedback  
65 through energy, water, and carbon cycles (Cheng et al., 2022a; Trenberth, 2022; von  
66 Schuckmann et al., 2016). Substantial changes in ocean temperatures also profoundly  
67 impact ocean biogeochemical processes and ecosystems and are critical for ocean health  
68 and human society (Bindoff et al., 2019; Cheng et al., 2022a).

69 Many gridded T/OHC datasets have been produced by independent groups, and most  
70 of them are updated annually or more frequently (Cheng et al., 2022a; Good et al., 2013;  
71 Hosoda et al., 2008; Ishii et al., 2017; Levitus et al., 2012; Li et al., 2017; Meyssignac et  
72 al., 2019; Roemmich and Gilson, 2009). Most widely-used products are at  $1^\circ \times 1^\circ$   
73 horizontal resolution and monthly temporal resolution from near-surface to at least 2000 m  
74 depth. Some products utilize all available *in situ* observations and span at least half a  
75 century, prominent examples being the data products compiled by the Institute of  
76 Atmospheric Physics (IAP) (Cheng and Zhu, 2016; Cheng et al., 2017) from 1940-present;  
77 Japan Meteorological Agency (JMA) (Ishii et al., 2017) from 1955-present; National  
78 Centers for Environmental Information (NCEI), National Oceanic and Atmospheric  
79 Administration (NOAA) from 1950-present (Levitus et al., 2012); and University of  
80 California since 1949 (Bagnell and DeVries, 2021). As Argo data has achieved near-global  
81 upper 2000 m open ocean coverage since ~2005, many Argo-based or Argo-only gridded  
82 products are available. Examples include gridded products from SCRIPPS after 2004  
83 (Roemmich and Gilson, 2009); China Argo Real-time Data Center since 2005 (Li et al.,  
84 2017); and Copernicus since 2005 (von Schuckmann and Le Traon, 2011). These products  
85 usually span from ~2005 to the present for the upper ~2000 m. These data benefit from the  
86 high quality of Argo data but are not fully resolving polar regions, shallow waters, and  
87 regions with complex topography.

88 In 2016, the IAP group provided its first gridded product for the upper 700 m ocean  
89 (Cheng and Zhu, 2016) by merging all available observations since 1960. With a revised  
90 mapping method and a thorough evaluation process with synthetic observations, an update  
91 (IAP version 3, IAPv3) became available in 2017 for the upper 2000 m ocean with data



92 since the 1950s (Cheng et al., 2017). The IAPv3 has supported scientific research, climate  
93 assessment reports, and monitoring practices (Bindoff et al., 2019; Gulev et al., 2021;  
94 WMO, 2022).

95 After the release of IAPv3, there has been progress with observation data quality  
96 control and new/updated techniques for temperature data processing and reconstruction.  
97 For example, Gouretski et al. (2022) found that old Nansen cast bottle data contained  
98 systematic biases that impacted the T/OHC data before 1990. Revisions are also available  
99 to the bias corrections for the Mechanical Bathythermographs (MBT) and eXpendable  
100 Bathythermographs (XBT) data (Cheng et al., 2014; Gouretski and Cheng, 2020), mainly  
101 impacting the data within 1940–2005. Tan et al. (2023) developed a new quality-control  
102 system that advances the detection of outliers after accounting for the non-Gaussian  
103 distribution of local temperatures in determining the local climatological range. The impact  
104 of inhomogeneous vertical resolution of temperature profiles has been recognized  
105 previously (Cheng and Zhu, 2014) and received more attention recently (Li et al., 2020)  
106 with a new vertical interpolation approach (Barker and McDougall, 2020). Upgrading the  
107 product with new developments is important to better support the follow-on studies on  
108 climate assessments.

109 This manuscript discusses the revisions to the IAP ocean objective analysis product  
110 (IAPv4) since the publication of the IAPv3 (Cheng et al., 2017). The data and methods are  
111 introduced in Section 2 and the results are presented in Section 3, with analyses of the  
112 character of the IAPv4 on regional and global scales and at various time scales. The EEI  
113 and sea level budgets based on the new data product are also investigated. A summary and  
114 discussion are provided in Section 4, with some remaining issues and outlooks being  
115 discussed.

116

## 117 **2. Data and Methods**

### 118 **2.1 Data source**

119 The majority of the *in situ* measurements used to create the data product come from  
120 the World Ocean Database (WOD), downloaded in September 2023. Data from all  
121 instrument types are used, including XBTs (Goni et al., 2019), Argo (Argo 2000),  
122 Conductivity/Temperature/Depth profilers (CTDs), MBTs, bottles, moorings, gliders,  
123 Animal Borne Ocean Sensors (McMahon et al., 2021) and others (Boyer et al., 2018) (Fig.



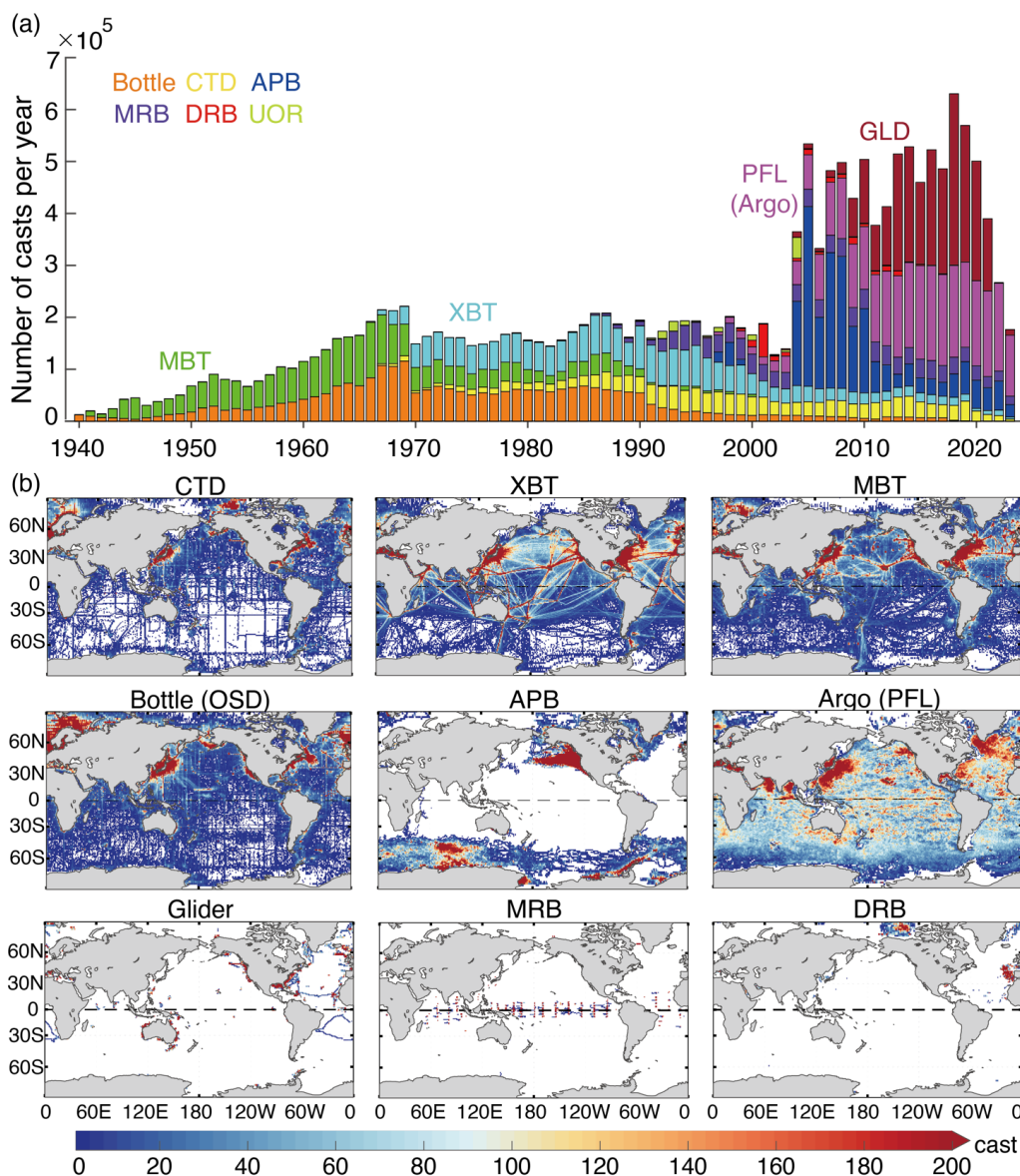
124 1). There is a total of 17,634,865 temperature profiles from January 1940 to September  
125 2023 (Fig. 1).

126 Argo data are processed following the recommendations of the Argo community.  
127 Adjusted data are used where applicable. Both Delayed- and Real-Time Argo data have  
128 been incorporated in IAPv4. As Real-Time Argo data have only passed automated, simple  
129 QC tests in real-time, these data may still contain temperature, pressure, and salinity values  
130 affected by unknown errors. However, through a sensitivity study, Cheng (2024) indicated  
131 that including Real-Time Argo data does not bias the OHC calculation for the IAP  
132 analysis. Nevertheless, IAP data are updated frequently (every 1-3 months): each time the  
133 updated Argo data is used, the T/OHC fields are recalculated following the  
134 recommendation by the Argo group (Wong et al., 2020). The data from the Argo floats in  
135 the “grey list” have been removed from the calculation (<https://data-argo.ifremer.fr/>).

136 To complement the WOD with relatively less data in the Arctic and coastal regions of  
137 the Northwest Pacific, this paper also uses data from other sources. There are a total of  
138 85,990 additional temperature profiles, about 0.50% of the data, which is expected to  
139 improve the reconstruction in these data-sparse regions (compared with IAPv3 and other  
140 products).

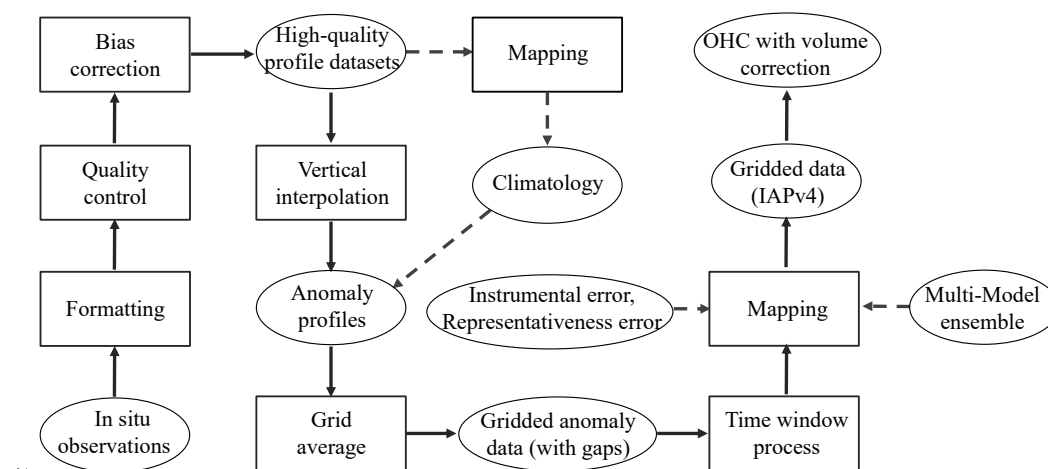
141 The *in situ* data have been processed as described in a flow chart in Figure 2. In the  
142 following sections, the key techniques of data processing are introduced.

143



144.  
 145.  
 146.  
 147.  
 148.  
 149.  
 150.  
 151.

**Figure 1: (a) Yearly number of temperature casts for different instruments; (b) number of subsurface temperature casts in 1-degree grid box from 1940 to 2023 collected by different instruments: CTD (Conductivity/Temperature/Depth), XBT (eXpendable BathyThermographs), MBT (Mechanical BathyThermograph), Bottle, APB (Animal mounted Pinniped Borne), PFL (Profiling Floats, i.e. Argo), Glider, MRB (Moored Buoy), and DRB (Drifting Buoy).**



151

153 **Figure 2: Flow chart of the IAP data reconstruction processes from the raw *in situ***  
 154 **observations to gridded data (IAPv4) and OHC estimates.** The ellipses indicate the data  
 155 (including data for error estimates), and the rectangle boxes show the techniques used to  
 156 process the data.

157

## 158 2.2 Data quality control

159 The quality control (QC) procedure aims to identify spurious measurements (including  
 160 outliers) and data with incorrect metadata through a set of quality checks and ensures the  
 161 quality of the *in situ* dataset (Tan et al., 2022). There is growing evidence that QC is  
 162 critical for accurate temperature/OHC reconstruction, as shown by Tan et al., (2023) where  
 163 two different QC systems produced a difference of approximately 15 % (~7 %) in the OHC  
 164 0-2000 m trend from 1955 to 1990 (2005-2021). Unfortunately, the impact of QC on OHC  
 165 estimates has not been evaluated in previous community-assessments on T/OHC  
 166 uncertainty (Boyer et al., 2016; Lyman et al., 2010). In this study, the QC procedure  
 167 follows the CAS-Ocean Data Center (CODC) Quality Control system, named CODC-QC  
 168 (Tan et al., 2023), where only the “good” data (flag=0) are used.

169 The CODC-QC system (Tan et al., 2023) has the following strengths, which make it  
 170 particularly suitable for T/OHC reconstruction:

- 171 1) A new local climatological range is defined in this CODC-QC system to identify  
 172 the outliers. Unlike many existing QC procedures, no assumption is made of a Gaussian  
 173 distribution law in the new approach, as the oceanic variables (e.g., temperature and



174 salinity) are typically skewed. Instead, the 0.5 % and 99.5 % quantiles are used as  
175 thresholds in CODC-QC to define the local climatological parameter ranges;

176 2) Local climatological ranges change with time to account for the long-term trends of  
177 ocean temperature accompanied by more frequent extreme events. Previously, the use of  
178 the static local ranges tended to remove too many “extreme events” associated with climate  
179 change in recent years that were actually real, leading to a QC-procedure related bias in the  
180 gridded dataset and OHC estimate (Tan et al., 2023);

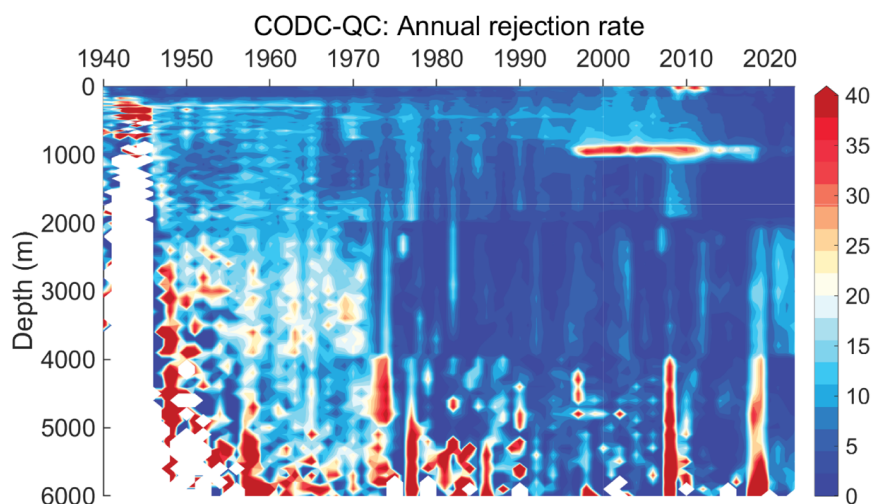
181 3) In addition, local climatological ranges for the vertical temperature gradient are  
182 constructed to account for the variability of ‘vertical shape’, increasing the ability of the  
183 scheme to identify spurious profiles;

184 4) The QC procedure is instrument-specific, accounting for characteristics inherent to  
185 particular instrumentation types. For example, XBT digital recording systems are allowed  
186 to continue to record beyond the rated terminal depth suggested by manufacturers (T7/DB  
187 probes below 760 m; T4/T6 below 460 m; T5 below 1830 m). Below the rated maximum  
188 depth, the XBT wire often breaks, leading to a characteristic change in recorded  
189 temperature values. The new QC procedure effectively identifies such profiles;

190 5) The thorough evaluation of the QC procedure performance and the application of  
191 the QC procedure to the manually QC-ed datasets demonstrated the effectiveness of the  
192 proposed scheme in removing spurious data and minimizing the percentage of mistakenly  
193 flagged good data.

194 Being applied to the entire temperature profile dataset the CODC-QC procedure  
195 identifies 6.22 % of all temperature measurements as outliers. The rejection rates  
196 (definition follows Tan et al., 2023) vary among instrumentation types (3.73 % for CTD,  
197 1.97 % for Argo, 12.06 % for XBT, 4.93 % for MBT, 6.54 % for bottle, 5.92 % for APB,  
198 4.54 % for DRB, 2.55 % for MRB). The overall percentage of outliers decreases over time  
199 from ~5 % in the 1940s to ~2.5 % in the 2020s, reflecting the progressive improvement of  
200 the instrumentation (Fig. 3). A rejection rate maximum (~12 %) during 2000~2010 is  
201 linked to the XBT data, which are especially abundant in the 800–1100m layer and are  
202 characterized by higher rejection rate below the maximum depth (Tan et al., 2023). The  
203 generally higher rejection rate below 4000 meters is related to the gross errors (such as  
204 measurements cooler than -2°C, big spikes, etc.) and the occurrence of the constant values  
205 (observations don’t change with depth). For example, the higher rejection rate within 2008-  
206 2010 below 4000 meters is because of the gross errors in the glider data.





207

208 **Figure 3: The rejection rate (%) after CODC-QC as a function of calendar year and**  
209 **depth.**

210

### 211 **2.3 Bias correction**

212 It is well known that data from several instrument types can exhibit biases both in  
213 temperature and depth. Temperature profiles obtained using XBTs and MBTs provide an  
214 example of biased data, especially because of uncertainties in the depth of measurement.  
215 Gouretski and Koltermann (2007) demonstrated their significant impact on the magnitude  
216 and variability of the global OHC estimates. That study triggered a series of publications  
217 where different bias correction schemes have been suggested for XBT (Gouretski and  
218 Reseghetti, 2010; Abraham et al., 2013; Cheng et al., 2016; Levitus et al., 2009; Wijffels et  
219 al., 2008), MBT (Gouretski and Cheng 2020; Levitus et al., 2009) and other instruments  
220 (Fig. 2). In the compilation of IAPv4, newly developed bias correction schemes are  
221 applied.

222 The XBT bias was found to be as large as  $\sim 0.1$  °C before 1980 on the global 0–700 m  
223 average, diminishing to less than 0.05 °C after 1990 (Gouretski and Koltermann 2007;  
224 Wijffels et al., 2008). Here, we use an updated XBT bias correction scheme (Cheng et al.,  
225 2014) to correct both depth and temperature biases in XBT data, following the community  
226 recommendation (Cheng et al., 2016; Goni et al., 2019). The depth and temperature biases  
227 depend on ocean temperature, probe type, and time. An inter-comparison among several



228 correction schemes rated the CH14 scheme the most successful (Cheng et al., 2018). Using  
229 XBT and collocated CTD data, we updated the CH14 scheme by re-calculating bias  
230 corrections between 1966-2016 and extending them for the years 2017 to 2023.

231 Comparison with collocated reference CTD profiles recently revealed significant  
232 systematic biases in the old hydrographic profiles obtained by means of Nansen bottle  
233 casts (Gouretski et al., 2022). Both depth and temperature measurements of bottle casts  
234 were found to be biased, and the proposed correction scheme was also implemented in  
235 IAPv4. The thermal bias is related to the time needed to bring the mercury thermometers in  
236 equilibrium with the ambient temperature after the completion of the hydrographic cast.  
237 The depth bias indicates an overestimation of the bottle depth due to the wire's deviation  
238 from the vertical position and is mostly related to the hydrographic casts where the  
239 thermometrical method of sample depth determination was not used. The correction  
240 scheme includes a constant thermal bias of  $-0.02$  °C and a depth- and time-variable depth  
241 bias.

242 The MBT bias is as large as  $0.28$  °C before 1980 for the global average and reduces to  
243 less than  $0.18$  °C after 1980 for the 0~200 m average. IAPv3 used (Ishii and Kimoto, 2009)  
244 (IK09) scheme to correct MBT bias, while a new scheme proposed by (Gouretski and  
245 Cheng, 2020) (GC20) is adopted in IAPv4. This shift is made because our assessment  
246 indicates the under-correction of MBT bias by the IK09 scheme within the upper 120 m  
247 and over-correction in the deeper layer, whereas GC20 corrects both depth and temperature  
248 biases. GC20 also found the MBT bias to be country-dependent, explained in terms of  
249 different instrumentation characteristics and working procedures. Therefore, the time-  
250 varying bias corrections are applied separately for the MBT profiles obtained by ships  
251 from the United States, Soviet Union/Russia, Japan, Canada, and Great Britain. Data from  
252 all other countries are corrected using a globally averaged correction.

253 Finally, thermal biases were recently reported for the data obtained by different kinds  
254 of data loggers attached to marine mammals (APB). Gouretski et al., (2024) analysed  
255 temperature profiles obtained between 2004 and 2019 in the high and moderate latitudes of  
256 both hemispheres. Comparison with the collocated reference CTD and Argo float data  
257 revealed a systematic negative thermal offset (average value  $-0.027$  °C) for mammal  
258 temperature profiles from SRDL (satellite-related data loggers). For the less accurate data  
259 from TDR (Temperature-Depth-Recorders), the comparison revealed a small positive  
260 temperature bias of  $0.02$  °C and the depth (pressure) bias indicating depth overestimation.



261

## 262 **2.4 Climatology**

263 For IAP and other data product generators, horizontal interpolation (mapping) is  
264 applied on a temperature anomaly field after removing a monthly climatology; thus, a pre-  
265 defined climatology field with an annual cycle is mandatory (Fig. 2). The accuracy of the  
266 climatology field is one of the key sources of uncertainty in reconstruction because the  
267 error in climatology will propagate into the anomaly field, impact the spatial dynamical  
268 consistency, and the accuracy of the reconstruction (Cheng and Zhu, 2015; Lyman and  
269 Johnson, 2014).

270 In IAPv4, the adjustive mapping procedure (see below) has been applied to  
271 reconstruct the climatology field (Table 1). The merit of using IAP mapping for  
272 climatology is its ability to better represent the spatial anisotropy of temperature variability  
273 (non-Gaussian distribution). Unlike IAPv3, where the 1990–2005 reference period was  
274 used, IAPv4 uses data between 2006 and 2020 to construct 12 monthly climatologies,  
275 taking advantage of more reliable data combined with better and more homogeneous  
276 spatial and temporal coverage in the last two decades (Table 1). Following the  
277 recommendation in Cheng and Zhu, (2015), a relatively short period of 15-year is used  
278 because climatology constructed with longer period of data will result in different baselines  
279 at different locations (i.e., the baseline shifted to earlier years in the middle latitudes of the  
280 North Hemisphere and the baseline shifted to more recent years in the Southern  
281 Hemisphere) and this inconsistency will violate the spatial structure of the anomaly field  
282 (Cheng and Zhu, 2015). Such a choice has been adopted by recent developments from  
283 other groups, such as Li et al., (2022).

284 IAPv4 used an 800 km influencing radii in climatology reconstruction, smaller than  
285 the 20° for IAPv3, to more properly account for the rapid change of temperatures with  
286 distance. There is a trade-off between data availability and the size of the influence radius.  
287 Using radii smaller than 500 km does not ensure a global fractional coverage (defined as  
288 the fraction of the total ocean area obtained by the mapping method) because of data  
289 sparseness (Cheng, 2024). As our tests suggest, using 500–800 km results in very similar  
290 reconstructions of climatology, therefore, 800 km is adopted.

291

## 292 **2.5 Vertical interpolation**



293           The vertical resolution of ocean temperature profiles changed dramatically over time  
294 associated with instrument evolution and the increase of data storage capability. For  
295 instance, the global mean vertical resolution at 500 m level changed from ~100 m in the  
296 1960s to less than 10 m during the 2010s (Li et al., 2020). Vertical interpolation of the raw  
297 profiles on standard levels is a critical process (Fig. 2): Cheng and Zhu (2014) indicated  
298 that the use of linear or spline vertical interpolation methods can bias the temperature  
299 reconstruction and OHC estimation (Barker and McDougall 2020; Li et al., 2020; Li et al.,  
300 2022). IAPv3 used the (Reiniger and Ross, 1968) (RR) method. Recently, Barker and  
301 McDougall (2020) proposed a new approach using multiple Piecewise Cubic Hermite  
302 Interpolating Polynomials (PCHIPs) to minimize the formation of unrealistic water masses  
303 by the interpolation procedure. The limitation of this method is that salinity data are  
304 needed for interpolation.

305           Because the largest difference between interpolation methods is found mostly for the  
306 low-resolution profiles (e.g., old Nansen casts), in practice, extremely low vertical  
307 resolution profiles had to be removed to reduce the uncertainty in interpolation. In IAPv4,  
308 this procedure is optimized compared to IAPv3, and only parts of profiles with a sufficient  
309 vertical resolution are used. The thresholds for the vertical resolution are empirically set by  
310 50 m in the upper 200m, 200m between 200 m and 1000 m, 500 m between 1000 m and  
311 2000 m, and 600m between 2000 m and 6000 m. As no interpolation method can  
312 adequately interpolate temperature for the vertical resolution beyond these thresholds,  
313 interpolation is not performed in such cases to avoid errors (these extreme low-resolution  
314 data are not used in further processing). Under this limitation for IAPv4, we still apply the  
315 RR method for temperature profiles.

316           Finally, IAPv4 extends the set of standard vertical levels with a total of 119 levels  
317 from 1 m to 6500 m (79 levels within the upper 2000 m) compared to 41 levels in IAPv3  
318 between 1 m and 2000 m (Table 1). The increase in vertical resolution is critical for  
319 accurately representing the mixed layer, as investigated below.

320

## 321 **2.6 Grid average and mapping**

322           The anomaly profiles are obtained by subtracting the monthly climatology from the  
323 vertically interpolated profiles. These anomalies are then averaged (arithmetic mean) into a  
324  $1^\circ \times 1^\circ$  grid at each standard level ( $1^\circ \times 1^\circ$  gridded average field) (Fig. 2). Due to the  
325 general data sparsity variable time windows (larger than one month) are used for monthly



326 reconstructions to ensure a truly global analysis. This process takes advantage of the  
327 persistence of anomalies, especially in the deep ocean, and thus is physically grounded.  
328 Specifically, after 2005, data within a three-month window are merged to provide a  
329 monthly reconstruction for each layer of the upper 1950 m. Before 2005, a time-varying  
330 and depth-varying time window is used, and it is generally smaller in the upper ocean and  
331 wider in the deeper ocean. Below 2000 m, a 5-year window is adopted.

332 Mapping interpolates the gridded (e.g., box-averaged) observations horizontally into a  
333 spatially complete map (Fig. 2) because not all  $1^\circ \times 1^\circ$  boxes are filled with data. (Fig. 2).  
334 IAPv4 adopted a similar mapping approach (Ensemble Optimal Interpolation with dynamic  
335 ensemble: EnOI-DE) as in IAPv3 introduced in Cheng and Zhu (2016) and Cheng et al.,  
336 (2017) but with the following modifications:

337 1) the largest influence radius has changed from  $20^\circ$  in the upper 700 m ( $25^\circ$  at 700–  
338 2000 m) in IAPv3 to 2,000 km in the upper 700 m (25,000 km at 700–6000 m) in IAPv4,  
339 to account for the reduced distance between two longitudes from tropics to the polar  
340 regions. This change mainly helps to improve the reconstruction in the high-latitude  
341 regions;

342 2) The three iterative runs are taken to effectively bring in different scales of  
343 variability with influencing radius changing from 2,000 km (25,000 km at 700–6000 m) to  
344 800 km and 300 km, respectively;

345 3) For each month, IAPv3 used 40 model simulations (historical runs with real  
346 forcings) from the Coupled Model Intercomparison Project phase 5 (CMIP5) to provide a  
347 flow-dependent ensemble, which is then constrained by observations to provide optimized  
348 spatial covariance. IAP mapping uses model-based covariance because we argue that  
349 spatial covariance can never be satisfactorily parametrized by some simple basic functions  
350 (such as Gaussian) given its complexity. With model-based, flow-dependent, and  
351 dynamically-consistent covariance, the IAP mapping provides a more realistic  
352 reconstruction than other approaches based on Gaussian-based parameterized covariance,  
353 as evaluated by many studies (Cheng et al., 2017; Cheng et al., 2020; Dangendorf et al.,  
354 2021; Nerem et al., 2018).

355 4) The observation error variance ( $\mathbf{R}$ ), which represents the error of the observations,  
356 is updated in IAPv4 as follows.  $\mathbf{R}$  consists of both the instrumental error ( $\mathbf{Re}$ ) due to  
357 inaccuracy and the representativeness error ( $\mathbf{Rr}$ ) due to the need to represent the spatial (at



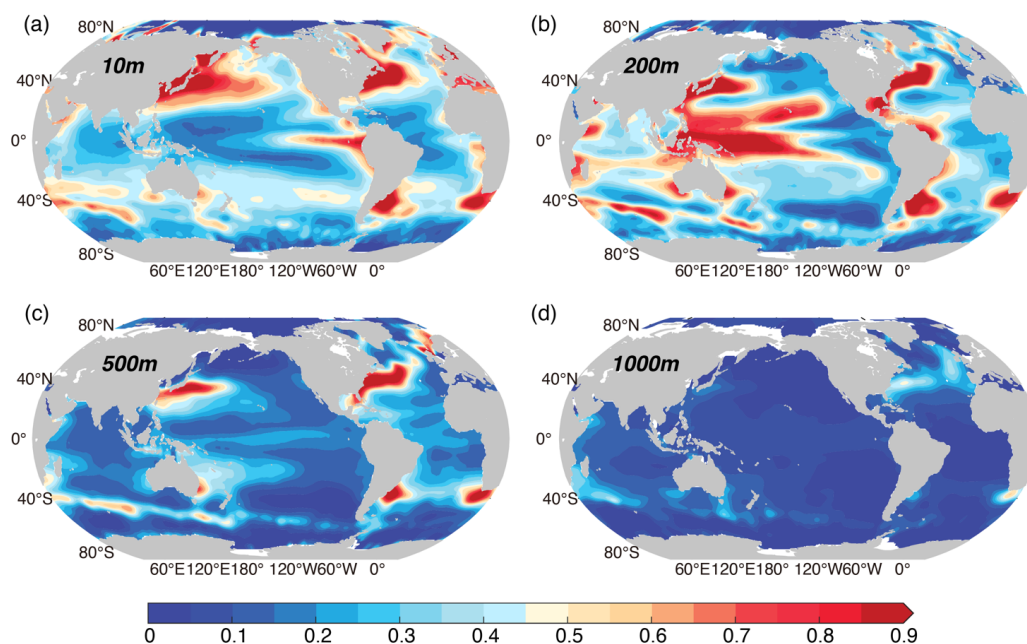
358 1° by 1° and 1 m standard grid depths) and temporal (1 month) averages from a limited  
359 numbered of observations (Cheng and Zhu, 2016):

$$360 \quad \mathbf{R} = \mathbf{R}_e + \mathbf{R}_r = (\sum_1^M \mathbf{E}i)/M + \sigma^2/M,$$

361 where M observations exist for a given grid cell.  $\mathbf{R}_e$  in each grid cell is set to the mean  
362 of the typical precision of the different instruments contributing data in the cell, which is  
363 set according to IQuOD (International Quality-Controlled Ocean Database) specification  
364 (Cowley et al., 2021).  $\sigma^2$  represents the variance of the various temperature measurements  
365 against the monthly mean value. The data from 2005 to 2022 are used to calculate  $\sigma^2$  in  
366 each grid because of greater data abundance and quality compared to earlier times.

367 As the representativeness error ( $\mathbf{R}_r$ ) is expected to be flow-dependent (i.e., the error is  
368 expected to be higher in areas with a large gradient of the flow speed and regions of higher  
369 variability), more observations are required to represent the mean value. Figure 4 shows a  
370 larger variance ( $\sigma^2$ ) in the boundary-current regions and near the Antarctic Circumpolar  
371 Current (ACC) in the upper ocean (e.g., 10 m, 200 m, 500 m). At 200 m, it shows a larger  
372  $\sigma^2$  in the Western Pacific Ocean, corresponding to the large thermocline variations at this  
373 layer. Below 1000 m, larger  $\sigma^2$  along the ACC frontal regions and in the North Atlantic  
374 Ocean occur because of a stronger mixing and convection in these regions.

375 The uncertainty in the derived gridded reconstruction is also based on the EnOI  
376 framework formulated by Cheng and Zhu, (2016). The uncertainty accounts for  
377 instrumental, sampling and mapping errors. Other error sources, including the choice of  
378 climatology, vertical interpolation, bias corrections, and QC, are not considered in this  
379 uncertainty estimate. Therefore, a more thorough uncertainty quantification method is  
380 needed, and this is under development in a separate study.



381

382

383

384

385

**Figure 4: Variance ( $\sigma^2$ ) of ocean temperature at several representative layers. (a)**

10 m, (b) 200 m, (c) 500 m and (d) 1000 m. The unit is degree Celsius.

**Table 1.** General information on IAPv4 and IAPv3 data products.

	IAPv3	IAPv4
<b>Horizontal resolution</b>	Global ( $1^\circ \times 1^\circ$ )	Global ( $1^\circ \times 1^\circ$ )
<b>Vertical levels</b>	41 levels from 1 m to 2000 m (1, 5, 10, 20, 30, 40, 50, 60, 70, 80, 90, 100, 120, 140, 160, 180, 200, 250, 300, 350, 400, 450, 500, 550, 600, 650, 700, 750, 800, 850, 900, 1000, 1100, 1200, 1300, 1400, 1500, 1600, 1700, 1800, 2000)	119 levels from 1 m to 6000 m (1, 5, 10, 15, 20, 25, 30, 35, 40, 45, 50, 55, 60, 65, 70, 75, 80, 85, 90, 95, 100, 110, 120, 130, 140, 150, 160, 170, 180, 190, 200, 220, 240, 260, 280, 300, 320, 340, 360, 380, 400, 425, 450, 475, 500, 525, 550, 575, 600, 625, 650, 675, 700, 750, 800, 850, 900, 950, 1000, 1050, 1100, 1150, 1200, 1250, 1300, 1350, 1400, 1450, 1500, 1550, 1600, 1650, 1700, 1750, 1800, 1850, 1900, 1950, 2000, 2100, 2200, 2300, 2400, 2500, 2600, 2700, 2800, 2900, 3000, 3100, 3200, 3300, 3400, 3500, 3600, 3700, 3800, 3900, 4000, 4100, 4200, 4300, 4400, 4500, 4600,



		4700, 4800, 4900, 5000, 5100, 5200, 5300, 5400, 5500, 5600, 5700, 5800, 5900, 6000)
<b>Time period and resolution</b>	1940–2022 (reliable data after 1955), monthly	1940–present (reliable data after 1955), monthly
<b>Quality-control</b>	WOD (Garcia et al., 2018)	CODC-QC (Tan et al., 2023)
<b>Vertical interpolation</b>	RR (Reiniger and Ross, 1968) interpolation	RR (Reiniger and Ross, 1968) interpolation
<b>Climatology</b>	IAP climatology: simple gridded average and then spatial interpolation with distance-weighted average	Improved IAP reconstruction with EnOI approach
<b>XBT bias correction</b>	CH14 (updated in 2018)	CH14 (revised and updated in 2023)
<b>MBT bias correction</b>	IK09 (Ishii and Kimoto, 2009)	GC20 (Gouretski and Cheng, 2020)
<b>APB bias correction</b>	None	GCR24 (Gouretski et al., 2024)
<b>Bottle bias correction</b>	None	GCT23 (Gouretski et al., 2022)
<b>Mapping</b>	EnOI-DE with influencing radius of 20, 8, 3 degrees, iteratively.	EnOI-DE with influencing radius of 2000, 800, 300 km, iteratively. Representative error updated with 2005–2022 observations.
<b>Uncertainty</b>	Given by EnOI framework accounting for instrumental error and horizontal sampling/mapping error	Given by EnOI framework accounting for instrumental error and horizontal sampling/mapping error
<b>DOI</b>	/	YES

386

### 387 **2.7 OHC calculation and volume correction**

388 Based on the gridded temperature reconstruction (Table 1), OHC in each grid is  
 389 calculated as  $OHC(x, y, z) = c_p \iiint_{V(x,y,z)} \rho T dV(x, y, z)$ . following TEOS-10 standards,  
 390 where  $c_p$  is a constant of  $\sim 3991.9 \text{ J (kg K)}^{-1}$  according to the new TEOS-10 standard  
 391 formulation as conservative temperature and absolute salinity are used,  $\rho$  is potential  
 392 density in  $\text{kg m}^{-3}$ , and  $T$  is conservative temperature measured in degrees Celsius (here it  
 393 is anomaly relative to the 2006–2020 baseline) (Cheng et al., 2022a).

394 As OHC is an integrated metric over a specific ocean volume, properly identifying  
 395 ocean volume is critical, especially in shallow waters. Previous studies found a 10–20 %





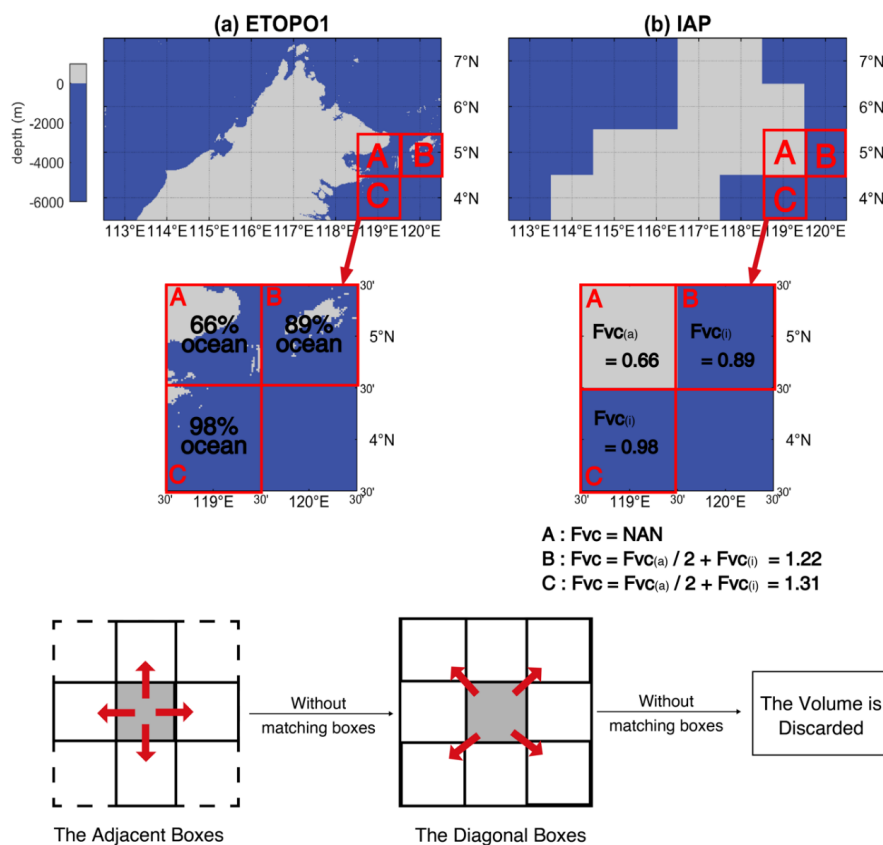
396 difference in the OHC trend in recent decades between different land-ocean masks (von  
397 Schuckmann and Le Traon, 2011). Specifically, in marginal sea areas with complex  
398 topography,  $1^\circ \times 1^\circ \times \Delta z$  grid boxes (where  $\Delta z$  is the depth range of the grid box) near  
399 coasts and islands typically cover both ocean and land areas but are assigned to represent  
400 land or ocean only. Thus, the gridded ocean temperature datasets are subjected to errors  
401 from inaccurate land-sea attribution. Here, we offer a volume correction (VC) for these  
402 grid boxes to improve the OHC estimate, as follows.

403 For each  $1^\circ \times 1^\circ \times \Delta z$  grid box, we introduce a VC factor (denoted as  $F_{VC}$ ) to correct  
404 the OHC values:  $OHC_{VC}(x, y, z) = OHC(x, y, z) \times F_{VC}(x, y, z)$ . First, we assume the  
405 seawater volume distribution in 1 arc-minute topographic data of ETOPO1 as “truth”. No  
406 correction is needed if a box is assigned to ocean according to ETOPO1 data, thus,  $F_{VC}=1$ .  
407 If a fraction of a  $1^\circ \times 1^\circ \times \Delta z$  grid box is land according to ETOPO1 and IAP data includes  
408 T/OHC values, the  $F_{VC}$  is represented by the fraction of the ocean volume in this box  
409 (illustrated in Fig. 5), and the volume for OHC calculations can be corrected with  $F_{VC}(i)$ . In  
410 a grid box, if there is no IAP data (i.e., it is land according to the IAP mask), but this box  
411 contains some ocean volume according to ETOPO1 data, we define  $F_{VC}(a)$  again as the  
412 fraction of the ocean volume in this box, and then this  $F_{VC}(a)$  is added to the adjacent grid  
413 boxes where there are values in IAP data. If all the adjacent grid boxes contain no data, the  
414 volume is equally redistributed to the diagonal boxes (Fig. 5). The volume is discarded if  
415 there is no data in all adjacent and diagonal boxes.

416 With this approach, the VC factor in each grid box is a sum of two components: a  
417 local adjustment  $F_{VC}(i)$  and a redistribution from the adjacent grids:

$$418 \quad F_{VC}(a): F_{VC} = F_{VC}(i) + F_{VC}(a),$$

419 To avoid misidentification of sea ice, we performed VC only on the global grid points  
420 within  $60^\circ S$  to  $60^\circ N$ . Eventually, we obtained a three-dimensional FVC that fits the IAP  
421 grids ( $119 \times 360 \times 180$ ; depth coverage to 6000 m) and used it to compute OHC. The VC  
422 applied to  $\sim 15\%$  of all the  $1^\circ \times 1^\circ \times \Delta z$  grid boxes of IAPv4 ocean grid boxes (with  $F_{VC} \neq$   
423 1) for the entire 0-6000 m ocean and  $\sim 10\%$  grid boxes of the upper 2000 m.



424

425 **Figure 5:** An example explaining the Volume Correction algorithm. (a) Bathymetry

426 derived from ETOPO1. (b) Bathymetry in IAPv4 analysis.

427

## 428 2.8 Independent datasets for comparison and evaluation

429 Four Sea Surface Temperature (SST) datasets are used to evaluate the upper-most  
 430 layer (1 m) of IAPv4, including Extended Reconstructed SST version 5 (ERSST5) (Huang  
 431 et al., 2017); Japan Meteorological Agency Centennial Observation-Based Estimates of  
 432 SSTs version 1 (COBE1) (Ishii et al., 2005), and its version 2: COBE2 (Hirahara et al.,  
 433 2014); Hadley Centre Sea Ice and Sea Surface Temperature dataset (HadISST) (Rayner et  
 434 al., 2003). The anomalies relative to a 2006-2020 average were computed by removing the  
 435 climatology. Measurements of SST are made *in situ* by means of thermometers or retrieved  
 436 remotely from infrared and passive microwave radiometers on satellites (Kennedy 2014;  
 437 O’Carroll et al., 2019). Satellite SST observations began in the early 1980s. *In situ* SST



438 observations go back to the 19<sup>th</sup> century and involve many different measurement methods,  
439 including wooden and later insulated metal buckets to collect water samples, engine room  
440 inlet measurements, and sensors on moored and drifting buoys (Kennedy 2014). The  
441 subsurface temperatures are collected as “profiles” which contain multiple measurements  
442 at discrete vertical levels. Because of the differences in observation systems, SSTs are  
443 fundamentally different in their temporal and spatial coverage and temporal extent  
444 compared to subsurface observations on which OHC estimates rely. SST measurements  
445 also have different uncertainty sources and error structures; thus, the two systems are  
446 typically treated as independent data sources and have been used for cross-validation  
447 (Gouretski et al., 2012).

448 The capability of the new product to close the sea level budget and the Earth’s energy  
449 budget also provides tools for validation. A superior dataset should be capable of closing  
450 the sea level and the Earth’s energy budgets. The total sea level change has been monitored  
451 via satellite altimetry since 1993 (from the University of Colorado  
452 <https://sealevel.colorado.edu/>). The ocean mass change is derived from JPL RL06.1Mv3  
453 Mascon Solution GRACE and GRACE-FO data since 2002 (Watkins et al., 2015). For  
454 long-term total sea level change since the 1950s, we use a tide-gauge-based reconstruction  
455 (Frederikse et al., 2020). During the same period, the estimates of the Greenland ice sheet,  
456 Antarctic ice sheet, land water storage, and glacier ice melt contributions from Frederikse  
457 et al., (2020) are used to derive ocean mass change.

458 For the energy budget, the ice, land, and atmosphere heat content changes are from  
459 (von Schuckmann et al., 2023) from 1960 to the present. Because of the less reliable data  
460 before the 1990s for land, sea ice and ice sheets, the other set of land–atmosphere–ice data  
461 from 2005–19 is used as in Trenberth, (2022) to investigate the recent changes. The net  
462 radiation change at the top of the atmosphere is based on CERES EBAF data from Loeb et  
463 al., (2021) and Loeb et al., (2018) and Deep-C data from the University of Reading (Liu  
464 and Allan, 2022; Liu et al., 2017).

465 Several gridded ocean T/OHC gridded products are used here for inter-comparison,  
466 including the IAPv3 (Cheng et al., 2017), the EN4 ocean objective analysis product from  
467 the UK Met Office Hadley Centre (Good et al., 2013); the ocean objective analysis product  
468 (Ishii et al., 2017) (termed “ISH” hereafter) from JMA, and an Argo-only gridded product  
469 from SCRIPPS (Roemmich and Gilson, 2009) (termed “RG” hereafter).

470



## 471 **2.9 Trend calculation and uncertainty estimates**

472 The trends in this study have been estimated by a LOWESS approach (Cheng et al.,  
473 2022b), i.e., we apply a locally weighted scatterplot smoothing (LOWESS) to the time  
474 series (25-year window, equal to an effective 15-years smoothing), and then the OHC  
475 difference between the first and the end year is used to calculate the trend. This approach  
476 provides an effective method to quantify the local trend by minimizing the impact of year-  
477 to-year variability and start/end points.

478 Throughout this paper, the 90 % confidence interval is shown. The uncertainty of  
479 trend also follows the approach in Cheng et al., (2022a) based on a Monte Carlo  
480 simulation. First, a surrogate OHC series is formed by simulating a new residual series  
481 (after removing the LOWESS smoothed time series) based on the AR(1) process and  
482 adding it to the LOWESS line. Then a LOWESS trendline is estimated for each surrogate.  
483 This process is repeated 1000 times, and 1000 trendlines are available. The 90 %  
484 confidence interval for the trendline is calculated based on  $\pm 1.65$  times the standard  
485 deviation of all 1000 trendlines of the surrogates. Secondly, the uncertainty in the rate of  
486 the OHC is estimated by the 1000 LOWESS trendlines: 1) calculating the rate based on the  
487 difference between the first and last annual mean value of the LOWESS trendline in a  
488 specific period; 2) calculating  $\pm 1.65$  times the standard deviation of the 1000 rate values.

489

## 490 **3. Results**

### 491 **3.1 Climatological annual cycle**

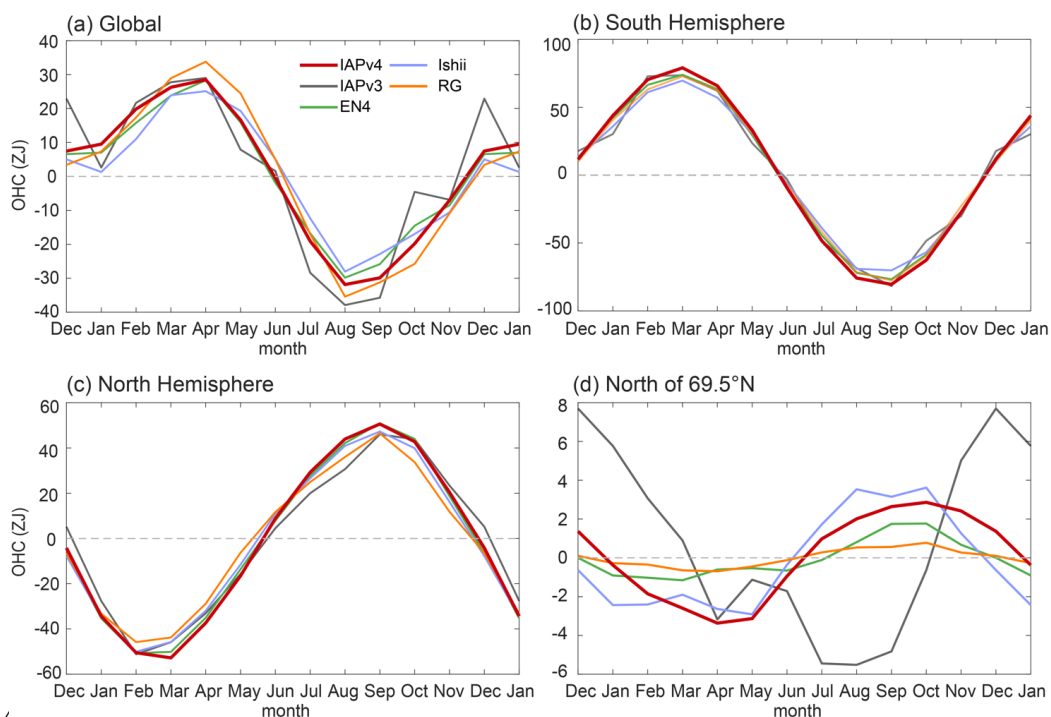
492 The annual cycle of the OHC above 2000 m of IAPv4 is compared with IAPv3, ISH,  
493 EN4, and RG (Fig. 6 and Fig. 7) for 2006–2020. There is a consistent annual cycle among  
494 different datasets for the global and hemispheric oceans. Globally, the ocean releases heat  
495 from boreal spring to autumn and accumulates heat from boreal autumn to spring, which is  
496 dominated by the southern hemisphere due to its larger ocean area (Fig. 6). The two  
497 hemispheres show opposite annual variations in OHC, associated with the annual change  
498 of solar radiation and different distribution of land and sea. For the global OHC above  
499 2000 m, IAPv4 shows a positive peak in April and a dip in August, with the magnitude of  
500 OHC variation of 60.4 ZJ for IAPv4 (66.9 ZJ for IAPv3), consistent with other datasets:  
501 53.2 ZJ for ISH, 58.1 ZJ for EN4, 69.2 ZJ for RG (where 1 ZJ =  $10^{21}$  J).

502 There are some unphysical variations in the OHC annual variations for IAPv3 (blue  
503 lines). For example, the global OHC shows large spikes in January and December, and a



504 big shift from September to October, by contrast, the other three data products show much  
505 smoother changes (Fig. 6a). The IAPv3 Arctic OHC (north of 69.5 °N) shows different  
506 phase change compared with the other datasets together with a big shift from September to  
507 December, and the magnitude of variability is much larger in IAPv3 than other datasets  
508 (Fig. 6d). The improvement in IAPv4 is mainly because of the methodology  
509 improvements: IAPv3 used 1990–2005 data to construct climatology which suffered from  
510 errors related to sparse data coverage, use of “degree distance” instead of “km distance”,  
511 and other error sources. Therefore, the IAPv4 analysis presents a physically tenable OHC  
512 seasonal variation.

513



514

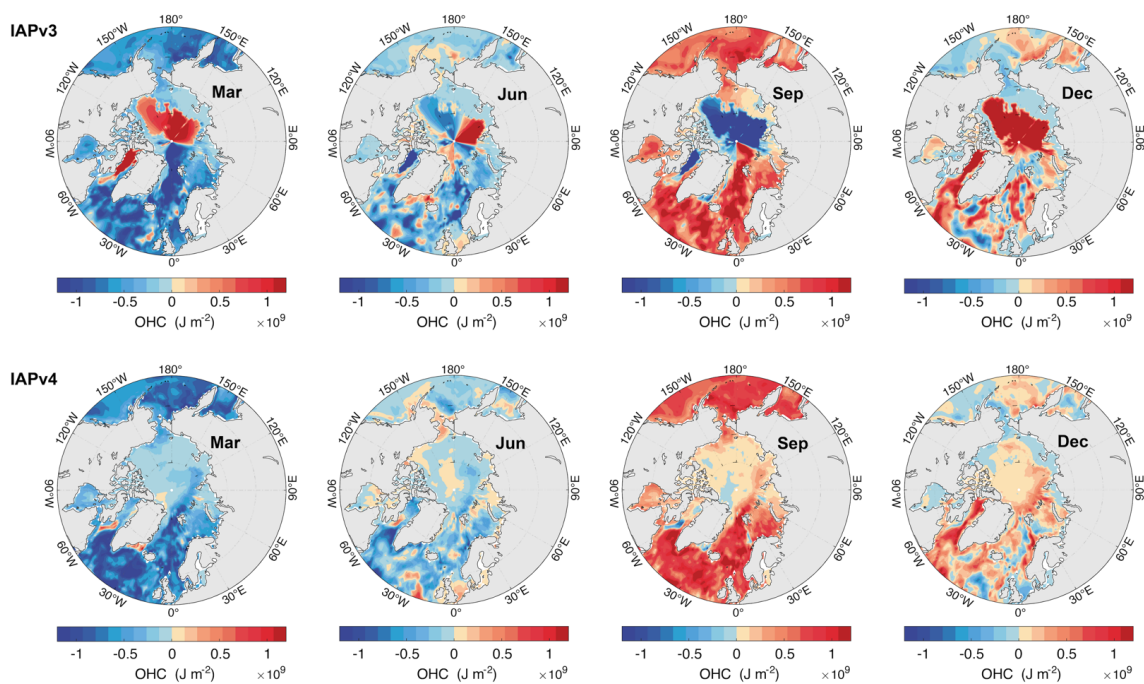
515 **Figure 6: Annual cycle of OHC of upper 2000 m for (a) the global oceans, (b) the**  
516 **Southern Hemisphere, (c) the Northern Hemisphere and (d) the oceans north of**  
517 **69.5°N. Five different data products are presented, including IAPv4 (red), IAPv3 (blue),**  
518 **ISH (purple), EN4 (green), and RG (orange).**

519

520 IAPv4 OHC data shows significant improvements in the Arctic region, reflected in  
521 both the spatial distribution and seasonal variation of OHC. In IAPv3, the maximum upper



522 2000 m OHC change occurs during December, however, for IAPv4, the maximum  
523 amounts to 2.9 ZJ in October and decreases to a minimum of  $-3.4$  ZJ in April. The spread  
524 of the OHC annual cycle in the Arctic region across different datasets is reduced from 5.2  
525 ZJ to 2.5 ZJ, indicating a smaller uncertainty. The spatial OHC anomaly distribution in the  
526 Arctic region of the IAPv4 is more spatially homogeneous than IAPv3, which seems not  
527 physical (Fig. 7). IAPv4 displays a consistent seasonal variation north of  $69.5^\circ\text{N}$  mainly  
528 because of the changes of the influencing radius from “degrees” to “kilometers”.



530 **Figure 7: Seasonal distribution of monthly OHC anomalies in the upper 2000 m**  
531 **in March, June, September, and December relative to the 2006 – 2020 annual mean.**

532 The top and lower panels are for IAPv3 and IAPv4 products, respectively.

533

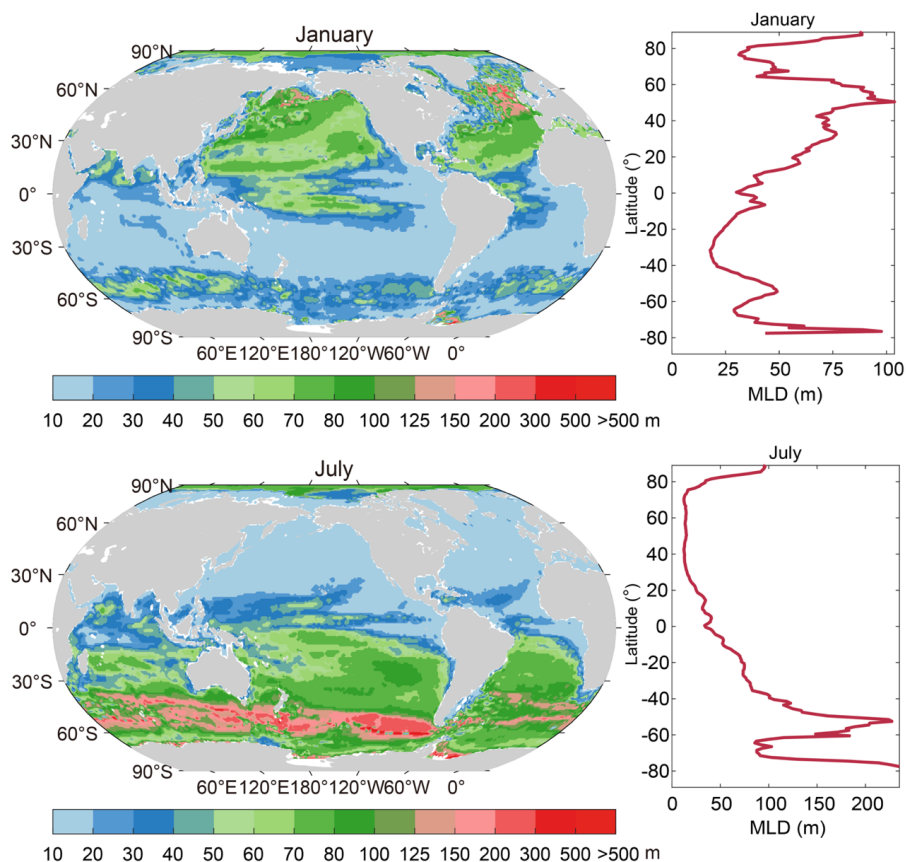
### 534 3.2 Mixed layer depth

535 Mixed layer depth (MLD) provides a crucial parameter of upper ocean dynamics  
536 relevant for upper-deeper ocean and air-sea interactions. Spatial distributions of the MLD  
537 in January and July are shown in Fig. 8 for IAPv4, based on criteria of  $\Delta T = 0.2^\circ\text{C}$   
538 temperature for the 10 m depth temperature. As expected, the seasonal variations of the  
539 MLD are generally opposite in the northern and southern hemispheres. The MLD shows a



540 much stronger seasonal variation in the subtropics and midlatitudes than in other regions  
541 (including the tropics), which is manifested as shallower MLD (~20 m) in summer due to  
542 strong surface heating that increases stratification, and deeper MLD in winter (>70 m)  
543 because of surface cooling and increased surface wind creating stronger mixing.

544 In the north hemisphere, the maximum MLD occurs during the wintertime in the  
545 subpolar North Atlantic deep water formation regions (40 °N ~ 65 °N), with values over  
546 500 m in the Norway Sea. In comparison, in the midlatitudes, the maximum of MLD is  
547 generally less than 125 m in the wintertime. The MLD minimum in the north hemisphere is  
548 in the summertime, and the values are mostly within 20 m depth. In the Southern  
549 Hemisphere, the MLD maximum values (deeper than 300 m) occur between 45 °S and  
550 60 °S of the Southern Ocean (north of the Antarctic Circumpolar Current) in the boreal  
551 summer where the year-round intense westerly winds are located. The minimum MLD in  
552 this region in the boreal winter is less than 70 m.. The seasonal variation of the MLD is  
553 well established by previous studies (Chu and Fan, 2023; de Boyer Montégut et al., 2004;  
554 Holte et al., 2017), and this evaluation confirms that IAPv4 temperature data is capable of  
555 reasonably representing the MLD.



556

557

558

559

560

561

562

### 3.3 Sea surface temperature

563

564

565

566

567

568

569

**Figure 8: Spatial pattern of the climatological mean MLD (left panels) and zonal mean MLD (right panels) in January (top) and July (bottom) estimated from the IAPv4.** Here, the MLD is calculated using the temperature difference criterion of  $\Delta T = 0.02$  °C between the surface and 10-meter depth.

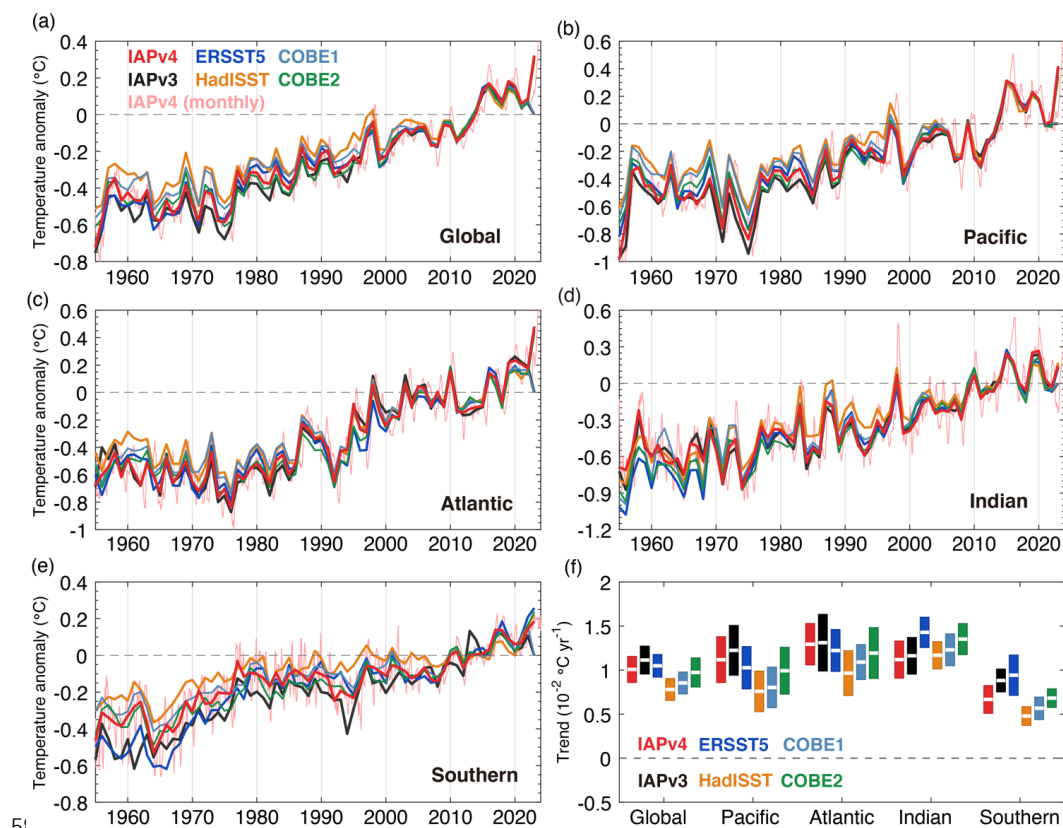
IAPv4 and IAPv3 temperature time series at 1 m depth (Fig. 9) are compared with four independent SST data products (ERSST5, HadISST, COBE1, and COBE2). All data products show robust sea surface warming in the global ocean and four main basins, and IAPv4 shows a quantitatively consistent warming rate since 1955 (Fig. 9). Since the HadISST and COBE2 data did not include the year 2023, we compare the long-term SST trend during 1955–2022 using these products (Fig. 9f). The global-mean IAPv4 SST rate between 1955 and 2022 is  $1.01 \pm 0.15$  °C century<sup>-1</sup> (90 % CI), which is within the range of





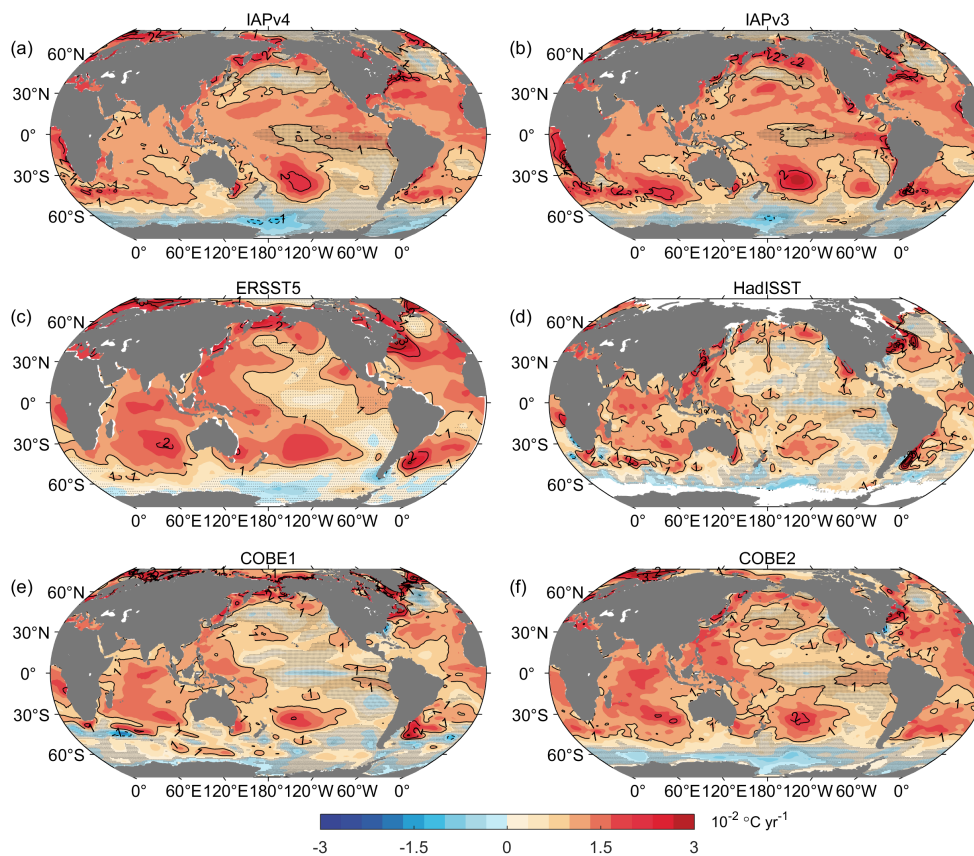
570 the SST products (ranging from 0.78 to 1.05 °C century<sup>-1</sup>). The 1955–2022 trend of IAPv4  
571 SST is slightly weaker than IAPv3 for the global ocean ( $1.11 \pm 0.16$  °C century<sup>-1</sup>) and all  
572 the ocean basins. The largest difference between IAPv4 and other SST products comes  
573 mainly from the Pacific and the Southern Ocean before 1980, associated with sparser  
574 observations.

575 The spatial distribution of long-term SST trends over the 1955–2022 period provides  
576 insights into the data consistencies and differences. First, IAPv4 shows a pattern of SST  
577 consistent with other datasets (Fig. 10). More rapid warming is found in the poleward  
578 western boundary currents regions, such as the East Australian Current and the Gulf  
579 Stream. The warmer ocean in the upwelling areas, such as the Tropical Eastern Pacific and  
580 Gulf of Guinea, are identified by all data products. The surface warming in the South  
581 Indian for IAPv4 data is weaker than for IAPv3, ERSST5, and COBE2 but is more  
582 consistent with HadISST and COBE1. The surface cooling in the south of 60 °S can also  
583 be found in all the datasets but with some discrepancies in magnitude and locations related  
584 to data sparsity.



586 **Figure 9: Global and basin time series of SST change for IAPv4, compared with**  
 587 **ERSST/HadISST/COBE1/COBE2 and IAPv3 from 1955 to present. (a) Global, (b)**  
 588 **Pacific, (c) Atlantic, (d) Indian and (e) Southern oceans (South of 30 °S) (units: °C). (f)**  
 589 **shows the warming rate from 1955 to 2022. The pink thin line is the monthly time series of**  
 590 **IAPv4 SST and other time series are annual time series of different datasets. The vertical**  
 591 **scales are different for different panels. All anomaly time series are relative to a 2006–**  
 592 **2020 baseline.**

593



594

595 **Figure 10: Spatial maps of the SST long-term trends during the 1955–2022 period.** (a)  
596 IAPv4, (b) IAPv3, (c) ERSST5, (d) HadISST, (e) COBE1 and (f) COBE2 (units:  $10^{-2} \text{ }^{\circ}\text{C}$   
597  $\text{yr}^{-1}$ ). The contour line interval is  $0.5 \times 10^{-2} \text{ }^{\circ}\text{C yr}^{-1}$ . The stippling indicates the regions with  
598 signals that are not statistically significant (90 % CI).

599

### 600 3.4 Global OHC time series

601 Global OHC time series for 0–700 m, 700–2000 m, 0–2000 m, and 2000–6000 m  
602 layers of IAPv4 (Fig. 11) for 1955–2023 versus IAPv3 show a robust ocean warming, with  
603 a linear warming rate of  $4.4 \pm 0.2 \text{ ZJ yr}^{-1}$  (0–700 m),  $2.0 \pm 0.1 \text{ ZJ yr}^{-1}$  (700–2000 m), and  
604  $6.4 \pm 0.3 \text{ ZJ yr}^{-1}$  (0–2000 m). The long-term warming revealed by IAPv4 is greater than  
605 IAPv3 ( $4.1 \pm 0.2 \text{ ZJ yr}^{-1}$  for 0–700 m,  $1.9 \pm 0.1 \text{ ZJ yr}^{-1}$  for 700–2000 m and  $6.0 \pm 0.3$   
606  $\text{ZJ yr}^{-1}$  for 0–2000 m). Before ~1980, bottle bias correction reduces the time-varying  
607 systematic warm bias in Nansen bottle data and leads to a stronger warming rate from

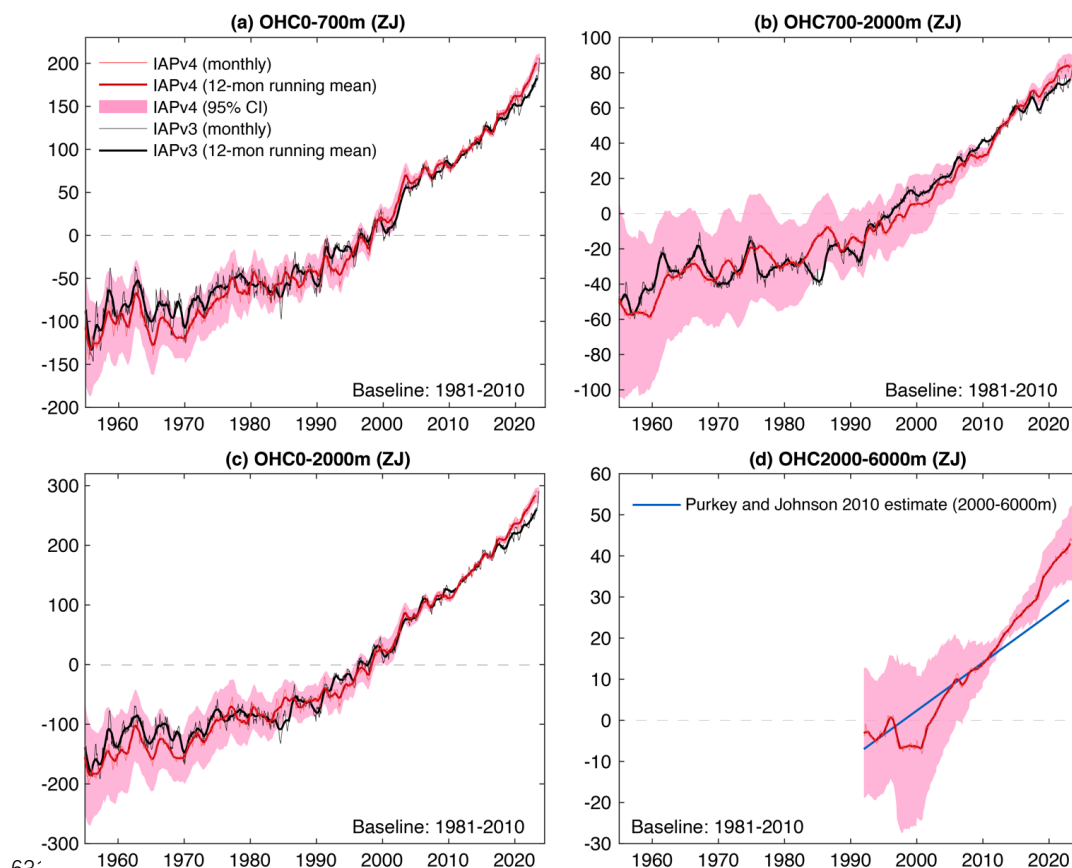


608 1955–1990. The updated MBT and XBT corrections are mainly responsible for the  
609 difference between 1980 and 2000. Data QC impacts the month-to-month variation of the  
610 OHC time series.

611 From 2005–2023, the new IAPv4 product shows stronger warming than IAPv3. The  
612 mean upper 2000 m warming rate is  $10.7 \pm 1.0$  ZJ yr<sup>-1</sup> for IAPv4 and  $9.6 \pm 1.1$  ZJ yr<sup>-1</sup> for  
613 IAPv3 (Fig. 11), mainly because of the replacement of the WOD-QC system by the new  
614 CODC-QC system in IAPv4. Tan et al., (2023) indicated that the WOD-QC system had  
615 removed more extreme higher temperature values in the regions of warm eddies and  
616 marine heat waves than CODC-QC. The IAPv3 700–2000 m OHC shows a much bigger  
617 drop in 2018 than IAPv4 (Fig. 11b), while the IAPv4 indicates an approximately linear  
618 700–2000 m warming since 2005, resulting in stronger 700–2000 m warming in IAPv4  
619 ( $3.6 \pm 0.5$  ZJ yr<sup>-1</sup>) than in IAPv3 ( $2.9 \pm 0.5$  ZJ yr<sup>-1</sup>).

620 Since the 1990s, the World Ocean Circulation Experiment (WOCE) provided a global  
621 network of abyssal ocean observations, sustained by repeated hydrological lines and a  
622 deep-Argo program (Katsumata et al., 2022; Roemmich et al., 2019; Sloyan et al., 2019).  
623 These high-quality data provide an opportunity to estimate deep OHC changes below 2000  
624 m. IAPv4 provides a new OHC estimate below 2000 m by collecting 5 years of data  
625 centered on each month. The result (Fig. 11d) indicates a robust abyssal (2000–6000 m)  
626 ocean warming trend since ~1993 of  $2.0 \pm 0.3$  ZJ yr<sup>-1</sup>. This is higher (within the  
627 uncertainty range) than the previous estimate of  $1.17 \pm 0.5$  ZJ yr<sup>-1</sup> in Purkey and Johnson  
628 (2010) but consistent with the recent assessment showing the acceleration of deep ocean  
629 warming in the Southwest Pacific Ocean (Johnson et al., 2019).

630



631  
632 **Figure 11: Global OHC time series for 0–700 m (a), 700–2000 m (b), 0–2000 m (c) and**  
633 **2000–6000 m (d).** All time series are relative to a 1981–2010 baseline. The shading  
634 indicates the 90 % confidence interval. The vertical scales are different for different panels.  
635 The unit is ZJ.

636  
637 Another feature of IAPv4 is the suppression of month-to-month noise compared to  
638 many available data products. Trenberth et al. (2016) noted that the month-to-month  
639 variation (quantified by the standard deviation of the monthly  $dOHC/dt$  time series) in all  
640 *in situ*-based OHC records is much larger than implied by the CERES records, suggesting  
641 that the OHC variation on this time scale is most likely spurious. Therefore, the magnitude  
642 of the month-to-month variation in the OHC record can be used as a benchmark of the data  
643 quality. The standard deviation of the CERES record is  $0.67 \text{ Wm}^{-2}$  from 2005 to 2023  
644 (Loeb et al., 2018). While IAPv4, IAPv3, ISH, EN4, BOA, NCEI, and SIO data show a



645 standard deviation of  $dOHC/dt$  time series of 3.52, 3.52, 7.49, 8.79, 10.05, 11.29, 10.00  
646  $Wm^{-2}$ , respectively (Table 2). Note that differentiation to get the rate of change amplifies  
647 noise, and applying a 12-month running smoother significantly knocks down the noise so  
648 that the IAPv4 standard deviation becomes  $0.75 Wm^{-2}$ , the smallest among the datasets  
649 investigated in this study (Table 2) and is the most physically plausible time series from  
650 this noise-level perspective.

651

652 **Table 2. Characteristics of Month-to-month variation of OHCT compared with**  
653 **CERES.** Comparisons of different ocean gridded products: the monthly standard deviation  
654 (std dev) of the monthly rates of change of OHC ( $Wm^{-2}$ ); the corresponding standard  
655 deviation of the 12-month running mean (13-points are used, with start-point and endpoint  
656 weighted by 0.5), and the linear trend with 90% confidence limits ( $Wm^{-2}$ ) (global surface  
657 area). The values are for 2005–2022.

Source	Std dev	Std dev (12 month)	Trend
IAPv4	3.52	0.75	$0.66 \pm 0.04$
IAPv3	3.52	0.79	$0.56 \pm 0.03$
ISH	7.49	1.35	$0.63 \pm 0.05$
EN4	8.79	1.03	$0.67 \pm 0.04$
BOA	10.05	1.16	$0.60 \pm 0.07$
NECI	11.29	1.11	$0.61 \pm 0.07$
SIO	10.00	1.24	$0.56 \pm 0.08$
CERES	0.67	0.33	

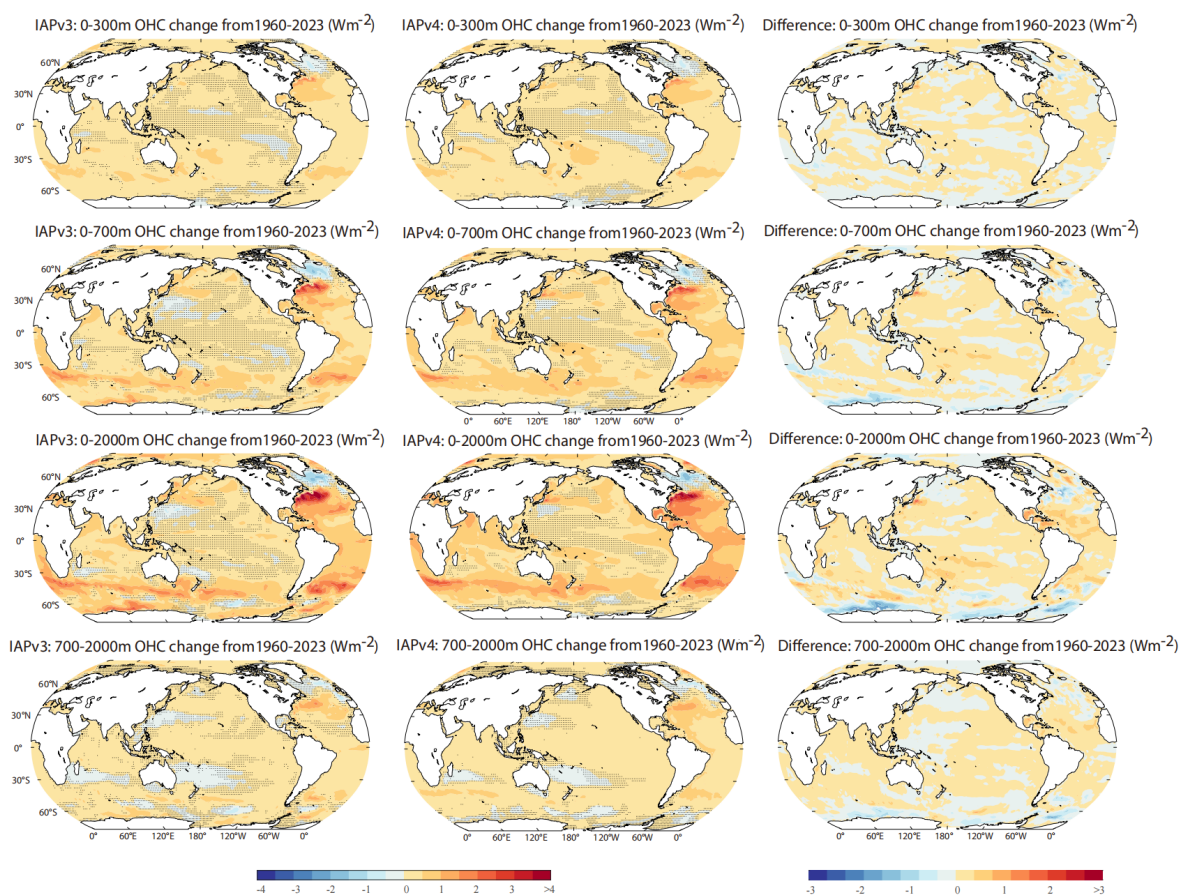
658

### 659 3.5 Regional OHC trends

660 For 1960–2023 (Fig. 12), the IAPv4 trends are slightly weaker than IAPv3 in the  
661 Pacific Ocean but slightly higher in the Atlantic Ocean (Fig. 12), with more than 95 % of  
662 the ocean area showing a warming trend. The polar regions also show remarkable  
663 differences compared to IAPv3, mainly because of the change of covariance, which  
664 improves the spatial reconstruction in the polar regions. The IAPv4 shows stronger  
665 warming near the boundary currents regions, mainly because of the improved QC that does  
666 not flag high-temperature anomalies. Nevertheless, the pattern of trends is very similar in  
667 the two versions of data, indicating the robustness of the ocean warming pattern. The  
668 Atlantic Ocean (within  $50^{\circ}S$ – $50^{\circ}N$ ) and the Southern Ocean store more heat than the



669 other basins, probably associated with the deep convection and subduction processes  
670 effectively transporting heat into the deep layers (Cheng et al., 2022a). The cold spots  
671 mainly include the Northwest Pacific and subpolar North Atlantic Ocean. In particular, the  
672 so-called “warming hole” in the subpolar North Atlantic Ocean can extend to at least 800  
673 m and is responsible for decreased OHC in this region. Some studies have linked this  
674 fingerprint to the slowdown of AMOC (Rahmstorf et al, 2015; Caesar et al., 2018).

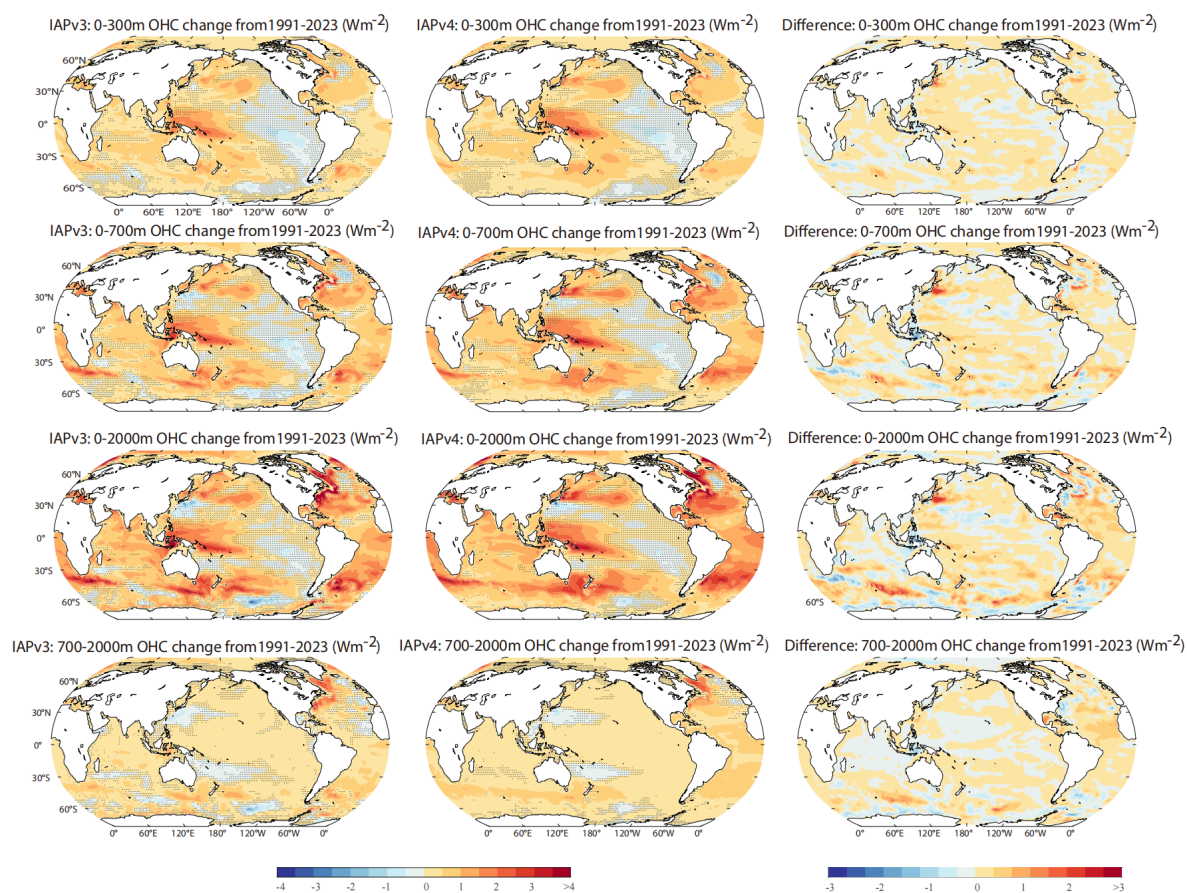


676 **Figure 12: Spatial pattern of the OHC trends for 0–300 m, 0–700 m and 0–2000 m,**  
677 **700–2000 m from 1960 to 2023.** The left panels show IAPv3, the middle panels are  
678 IAPv4; the right panels are the difference between IAPv4 and IAPv3.

679 For 1991–2023 (Fig. 13), the IAPv4 and IAPv3 pattern is also consistent. A La Niña-  
680 like trend appears in the Pacific for the 0–300 m, 0–700 m, and 0–2000 m OHCs. There is



681 a contrast between the warming trend of the tropical western Pacific and the cooling trend  
682 of the tropical eastern Pacific. Some studies have linked this pattern to the natural climate  
683 mode (Pacific Decadal Variability) (England et al., 2014), but some suggest it is a forced  
684 change driven by greenhouse gas increases (Fasullo and Nerem, 2018; Mann, 2021).  
685 Below 700 m, the 1960–2023 and 1991–2023 trend patterns are similar because deep  
686 ocean warming mainly occurs after 1990. Broad warming in most regions, but subtropical  
687 oceans in the West Pacific and South Indian oceans show a cooling, which is likely related  
688 to the subtropical gyre expansion and intensification (Zhang et al., 2014).



690 **Figure 13: Spatial pattern of the OHC trends for 0–300 m, 0–700 m, 0–2000 m and**  
691 **700–2000 m from 1991 to 2023. The left panels show IAPv3, the middle panels are**  
692 **IAPv4; the right panels are the difference between IAPv4 and IAPv3.**



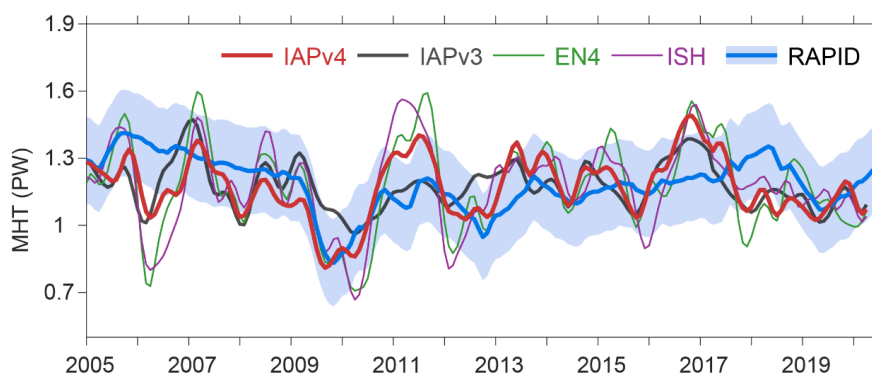


693

### 694 **3.6 Ocean meridional heat transport**

695       The ocean accounts for about one-third of the meridional heat transport (MHT). Thus,  
696 its change and stability are key to the climate system and its variability. The direct  
697 observations of ocean MHT are only possible in several cross-basin sections such as  
698 RAPID. The ocean MHT can be derived indirectly from the OHC and air-sea heat flux data  
699 (Trenberth and Fasullo, 2017; Trenberth et al., 2019). The comparison between OHC-  
700 derived MHT and RAPID data allows one to check the consistency among various  
701 observations. Here, we calculate the Atlantic MHT from April 2004 to December 2022  
702 using IAPv4 OHC and air-sea net heat flux data ( $F_s$ ) derived by TOA net energy flux and  
703 atmospheric heat divergence (Fig. 14).  $F_s$  is an average of three available products  
704 including MAYER2021 (Mayer et al., 2021) TF2018 (Trenberth et al., 2019) and the  
705 DEEP-C Version 5.0 from Reading University (Liu and Allan, 2022; Liu et al., 2020). The  
706 data are adjusted following Trenberth et al., (2019) approach to ensure zero MHT on the  
707 Antarctica coast. The inferred time series of MHT at 26.5 °N from other OHC data sets  
708 (IAPv3, Ishii, and EN4) are also shown in Fig. 14, compared with the RAPID observations  
709 (Johns et al., 2023).

710       The Inferred long-term mean (April 2004–December 2022) MHT from the updated  
711 IAPv4 OHCT (solid red line with the mean transport of 1.18 PW) is identical to the  
712 RAPID observation of  $1.18 \pm 0.19$  PW. Different OHC datasets cause different inter-  
713 annual variability in the MHT. It is shown that, from 2008 to 2020, the RAPID MHT  
714 agrees best with the IAPv4 estimates with a correlation of 0.52. By comparison, the  
715 correlation coefficients between RAPID and IAPv3, EN4, and Ishii are 0.33, 0.51, and  
716 0.49, respectively. Over the entire period of 2005~2022, the IAPv4 lies mostly within the  
717 RAPID uncertainty envelope.



718

719 **Figure 14: Derived Meridional heat transport at 26.5 °N.** The 12-month running mean  
720 northward MHT across 26.5 °N of different data sets compared with results from the  
721 RAPID array in PW. The error bars for RAPID in grey are  $1.64 \sigma$ .

722

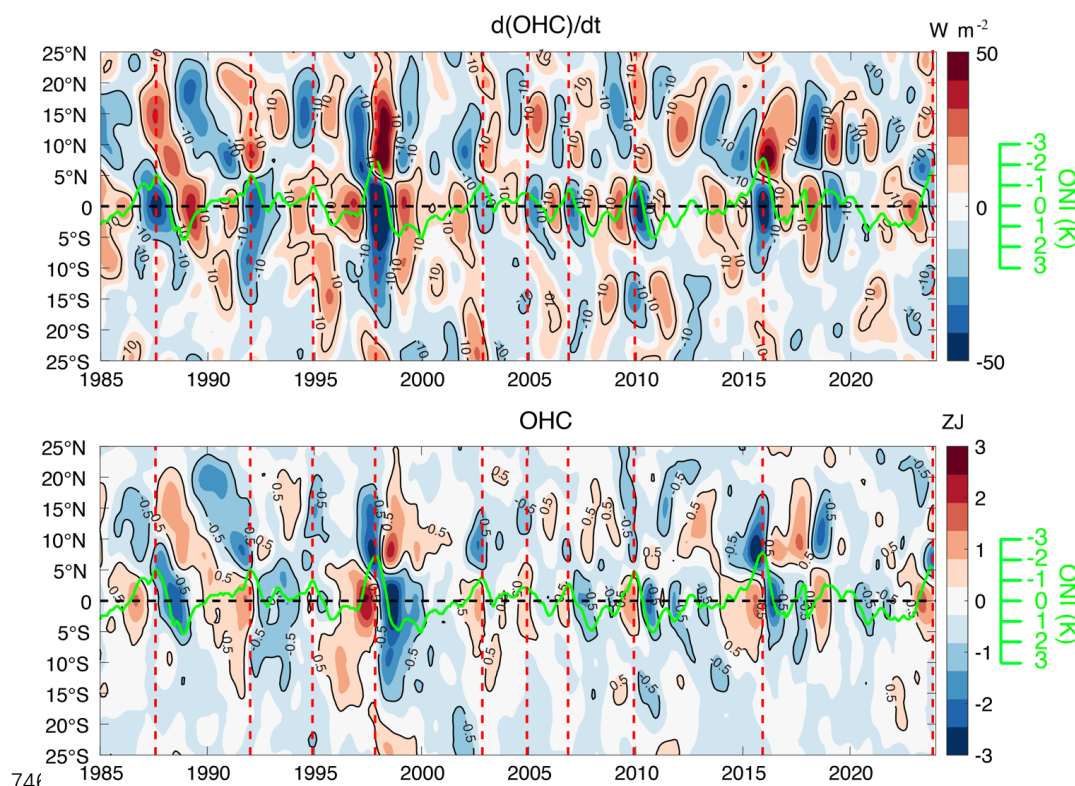
### 723 3.7 Inter-annual variability

724 The year-to-year variation of OHC is strongly influenced by ENSO from global to  
725 regional scales (Cheng et al., 2019; Roemmich and Gilson, 2011). To demonstrate the  
726 change of OHC associated ENSO, Figure 15 shows a Hovmöller diagram of the zonal  
727 upper 2000 m OHC and its change (time derivative of OHC:  $d(\text{OHC})/dt$ ) in the tropical  
728 Pacific Ocean from 1985 to 2023, compared with the Oceanic Niño Index (ONI). It is  
729 evident that both OHC and OHCT are closely correlated with ENSO.

730 Before the onset of El Niño events, there is an accumulation of heat ( $d(\text{OHC})/dt > 0$ )  
731 in the southern and equatorial tropical ocean region ( $20^\circ\text{S} - 5^\circ\text{N}$ ). The positive tropical  
732  $d\text{OHC}/dt$  leads ONI by  $\sim 15$  months (with peak correlation  $> 0.5$ ), making it a precursor of  
733 El Niño (Cane and Zebiak 1985; McPhaden, 2012; Lian et al., 2023). In contrast, heat is  
734 released ( $d(\text{OHC})/dt < 0$ ) from the tropics ( $20^\circ\text{S} - 5^\circ\text{N}$ ) to the North Hemisphere ( $5^\circ\text{N} -$   
735  $25^\circ\text{N}$ ) during and after El Niño (Cheng et al., 2019), with a maximum correlation  $> 0.8$  at 5  
736 months after the El Niño peak. The magnitude of the prominent change can reach up to 50  
737  $\text{Wm}^{-2}$  during the 1997–1998 and 2015–2016 extreme El Niño events. For the other  
738 moderate El Niño events, the regional OHC change varies around 10–20  $\text{Wm}^{-2}$  (Mayer et  
739 al., 2018). This typical heat recharge-discharge paradigm is crucial in ENSO evolution  
740 (Jin, 1997). Correspondingly, the zonal OHC anomalies show a warming state ( $\text{OHC} > 0$ )  
741 between  $\sim 20^\circ\text{N}$  and  $\sim 5^\circ\text{S}$  before the peak of El Niño events (with peak correlation  $> 0.7$  at  
742 5 months before El Niño peak), followed by a period of cooling ( $\text{OHC} < 0$ ) after the peak



743 of El Niño (with peak correlation  $>0.7$  at 12 months after El Niño peak). These variations  
744 are all physically meaningful and indicate that IAPv4 represents regional inter-annual  
745 variability, especially associated with ENSO.



747 **Figure 15:** Hovmöller diagrams illustrating the zonal mean (top) upper 2000 m  $d(OHC)/dt$   
748 ( $Wm^{-2}$ ) and (bottom) OHC (ZJ) in each  $1^{\circ}$  latitude band within  $25^{\circ}S \sim 25^{\circ}N$  in the  
749 tropical Pacific basin using IAPv4 data. The ONI is shown in green. Vertical dashed lines  
750 denote the peak time of each Niño event.

751

### 752 3.8 Ocean and Earth Energy Budget

753 The EEI provides a critical quantifier of the Earth's energy flow and climate change.  
754 It is also policy-relevant because it clearly shows the need to stabilize the climate system.  
755 With new T/OHC data, we re-assess the Earth's energy inventory since 1960. The land,  
756 atmosphere, and ice contributions are from the estimates obtained by von Schuckmann et  
757 al. (2023) for 1960-2023 and by Trenberth (2022) for 2015-2019.



758 It is evident that the earth has been accumulating heat since 1960. The Earth's heat  
759 inventory is  $512.9 \pm 65.0$  ZJ from 1960 to 2023 and  $251.5 \pm 14$  ZJ from 2005–2023. The  
760 upper 700 m ocean, 700–2000 m, 2000 m-bottom, land, ice, and atmosphere contribute to  
761 56.5%, 25.7%, 9.2%, 4.8%, 2.7%, and 1.1% of the total EEI, respectively, since 1960. The  
762 relative contribution has changed with time; for instance, since 1993, the contributions are  
763 55.2% (0–700 m ocean), 22.1% (700–2000 m ocean), 11.7% (2000 m–bottom ocean),  
764 3.7% (land), 2.8% (ice), and 1.0% (atmosphere). The land and ice contribution has  
765 increased in the recent two decades because of accelerated land and sea ice melting  
766 (Comiso et al., 2017; Hugonnet et al., 2021; Minière et al., 2024). From 2005–2019, more  
767 reliable land–atmosphere–ice datasets in Trenberth (2022) suggest a non–ocean  
768 contribution of 13.4 ZJ. Combined with the results for OHC with IAPv4, the EEI is 188.7  
769 ZJ with the ocean heat uptake of  $175.3 \pm 11$  for 2005–19, consistent with the value of  
770  $192.2 \pm 12$  ZJ using the non–ocean contribution data by von Schuckmann et al. (2023).

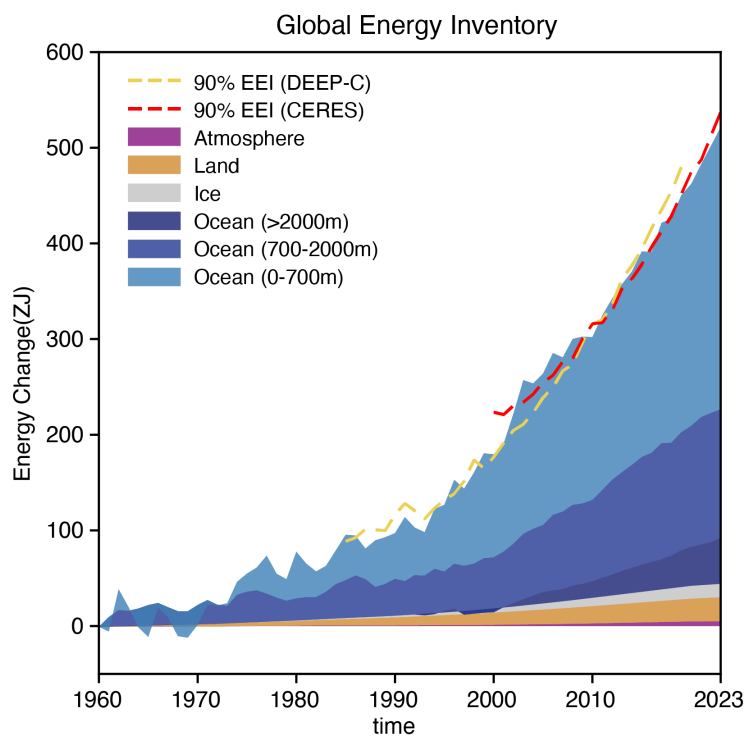
771 The derived energy inventory has been compared with satellite–based observations at  
772 the top of the atmosphere (TOA). Two comparisons are made: (1). integrate the TOA EEI  
773 to compare with the energy inventory (Fig. 16); (2) take the time derivative of the annual  
774 OHC to compare it with the TOA net radiation flux (Fig. 17).

775 The first approach avoids calculating the time derivative of OHC, which exacerbates  
776 noise in the time series. The net CERES change has been adjusted to  $0.71 \text{ Wm}^{-2}$  within  
777 2005–2015, here we adjust the trend of the integrated CERES data to the IAPv4 OHC  
778 trend to make it consistent and then compare the variability difference (Fig. 16). The  
779 RMSE between DeepC and IAP–OHC is 18.3 ZJ and 16.1 ZJ for CERES versus IAP–  
780 OHC. The comparison also indicates that the heat inventory shows a stronger heat increase  
781 from 2000 to 2005 but too slow heat accumulation during 2005–2010 compared with  
782 DeepC and CERES (Fig. 16). This might be due to the data gaps before the Argo network  
783 was fully established. DeepC and CERES show stronger heat accumulation since ~2015  
784 than the heat inventory, probably associated with the accelerated abyssal ocean warming  
785 found by the Deep-Argo program (Johnson et al., 2019). Furthermore, IAPv4 OHC shows  
786 a slightly higher (but consistent within the uncertainty range) Earth's heat uptake compared  
787 to von Schuckmann et al. (2023) results by 33.5 ZJ from 1960 to 2020, mainly because the  
788 correction of Nansen bottle biases and the updates of XBT and MBT biases in IAPv4 data.

789 The second approach to compare OHC with satellite–based EEI is to calculate the  
790 time derivative of OHC. To suppress the month–to–month noises, we estimate annual



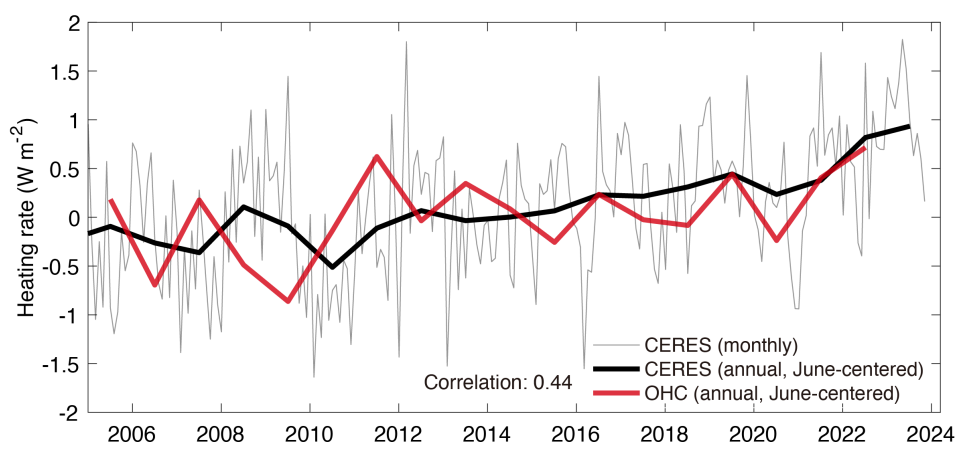
791 OHC based on one-year data centered on June (Fig. 17a) and December (Fig. 17b)  
792 separately, and then  $dOHC/dt$  is calculated with a forward derivative approach based on  
793 the annual time series. The annual mean of EEI time series is also used here for  
794 comparison (Fig. 17). The IAPv4 and CERES estimates show consistent inter-annual  
795 variability with a correlation of 0.44. The consistency gives higher confidence for the new  
796 IAPv4 data than IAPv3 (correlation of only  $\sim 0.15$ ). The trend of  $dOHC/dt$  is  $0.36 \text{ Wm}^{-2}$   
797  $\text{dec}^{-1}$  from 2005 to 2023, within the uncertainty range of the CERES record ( $0.50 \pm 0.47$   
798  $\text{Wm}^{-2} \text{dec}^{-1}$  in Loeb et al., 2021). However, it should be noted that the calculation of  
799  $dOHC/dt$  is sensitive to the choices of methods, data products, and time periods because of  
800 the noises and variability in the OHC time series. A careful analysis of the trend of  
801  $dOHC/dt$  (and EEI) is a research priority.



802  
803 **Figure 16: The global energy budget from 1960 to 2023.** The Atmosphere, land, and ice  
804 heat inventory is from von Schuckmann et al., (2023). Integrated EEI from DEEP-C  
805 (1985–2018) (Liu and Allan, 2022) and CERES (2001–2022) (Loeb et al., 2021) dataset  
806 are presented by dashed lines for comparison, with the trend adjusted to the IAP estimate  
807 to account for the arbitrary choice of integration constant.



808



809

810 **Figure 17: Annual ocean heating rate compared with CERES data.** Both annual OHC  
811 and CERES EEI data are centered on June. The long-term mean is removed for all-time  
812 series.

813

### 814 3.9 Steric sea level and sea level budget

815 The updated IAP data is used to re-assess the sea level budget for 1960–2022, 1991–  
816 2018, and 2002–2023. From 1960 to 2022, the sum of individual components ( $1.91 \pm 0.07$   
817  $\text{mm yr}^{-1}$ ) is consistent with the tide-gauge-based reconstruction ( $2.08 \pm 0.10 \text{ mm yr}^{-1}$ ) of  
818 the global mean sea level (GMSL) (Fig. 18). Based on our estimate, the steric sea level,  
819 Antarctic ice sheet, Greenland ice sheet, glaciers, and land water storage contribute to the  
820 total sea level with 48.2%, 9.4%, 19.4%, 27.2%, and -3.7%, respectively (Table 3).

821 From 1971 to 2018 (an assessment period for GMSL in IPCC-AR6), the sum of  
822 individual components ( $2.13 \pm 0.06 \text{ mm yr}^{-1}$ ) is consistent with a tide-gauge-based  
823 reconstruction ( $2.34 \pm 0.08 \text{ mm yr}^{-1}$ ) of global mean sea level (GMSL) (Fig. 18), with a  
824 difference of  $0.21 \text{ mm yr}^{-1}$ , a better closure than IPCC-AR6 (the residual is  $0.33 \text{ mm yr}^{-1}$ )  
825 (Table 3).

826 After 1993, when GMSL can be directly observed by altimetry, the sum of sea level  
827 components is  $3.11 \pm 0.11 \text{ mm yr}^{-1}$  (1993–2018), again, consistent with the altimetry-based  
828 sea level ( $3.26 \pm 0.16 \text{ mm yr}^{-1}$ ) considering the uncertainty (Fig. 18). The residual of the  
829 budget is  $0.16 \text{ mm yr}^{-1}$ , smaller than 1971–2018. Altimetry records suggest an acceleration  
830 of sea level rise from 1993 to 2018, ranging from 0.0535 (Frederikse et al., 2020) to 0.094



831  $\pm 0.012 \text{ mm yr}^{-2}$  (IPCC 2021; Nerem et al., 2018), and the difference might reveal the  
 832 uncertainty in bias correction and data processing for altimetry data. Here, the sum of  
 833 contributions shows a similar acceleration of  $0.0592 \pm 0.0196 \text{ mm yr}^{-2}$  (1993–2018),  
 834 indicating a robust acceleration of sea level rise since the 1990s.

835

836 **Table 3. Sea level budget is based on IAPv4 and previous studies.** The trends of IPCC  
 837 AR6 and (Frederikse et al., 2020) are based on least-squares fit. The trend of IAPv4 is  
 838 based on LOWESS method (Cheng et al., 2022b). The uncertainty of IPCC AR6 and  
 839 Frederikse et al. (2020) is given by the 90% confidence interval. The uncertainty of IAPv4  
 840 is based on a 90% confidence interval through the Monte Carlo method. The unit is  $\text{mm yr}^{-1}$ .  
 841 <sup>1</sup>.

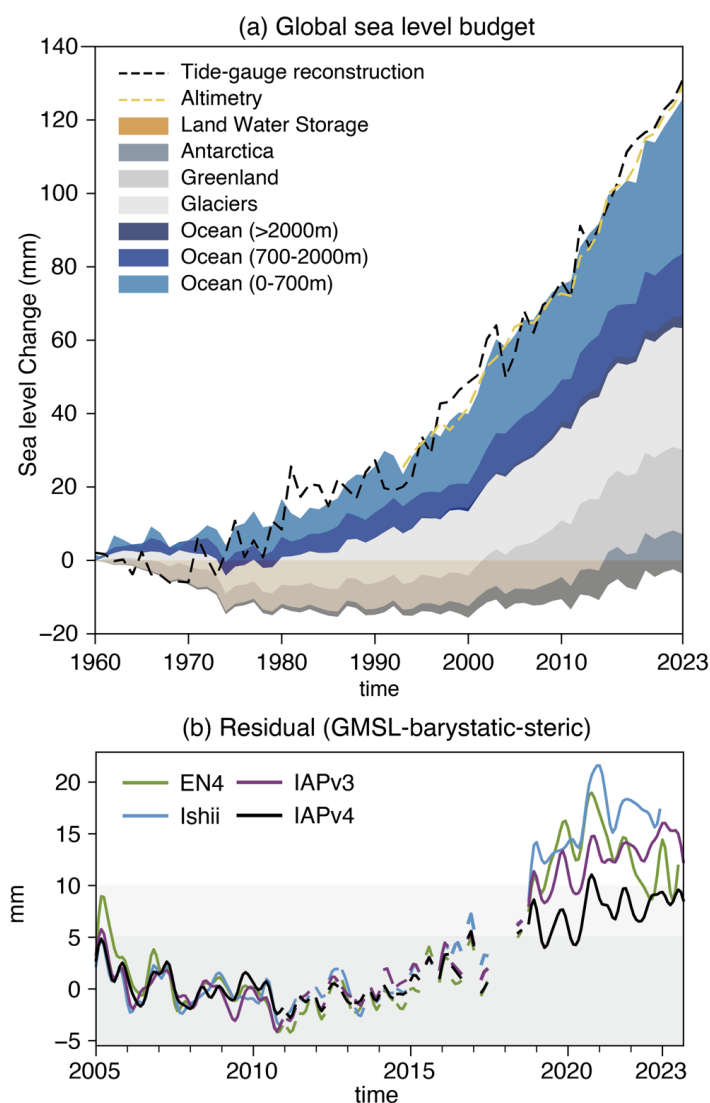
	1971–2018	1993–2018
<b>GMSL</b>		
IPCC AR6	2.33 [1.55, 3.12]	3.25 [2.88, 3.61]
(Frederikse et al., 2020)		3.35 [2.91, 3.82]
IAPv4	$2.34 \pm 0.08$	$3.26 \pm 0.16$
<b>Steric</b>		
IPCC AR6	1.01 [0.73, 1.29]	1.31 [0.95, 1.66]
(Frederikse et al., 2020)		1.19 [0.99, 1.44]
IAPv4	$0.97 \pm 0.05$	$1.27 \pm 0.09$
<b>Sum of contribution</b>		
IPCC AR6	2.00 [1.52, 2.49]	2.85 [2.41, 3.29]
(Frederikse et al., 2020)		3.16 [2.78, 3.57]
IAPv4	$2.13 \pm 0.06$	$3.11 \pm 0.11$
<b>Residual</b>		
IPCC AR6	0.33	0.40
(Frederikse et al., 2020)		0.19
IAPv4	0.21	0.15

842

843 After 2002, the GRACE satellite supported direct observation of barystatic sea level,  
 844 which is the sum of the sea level change due to the land water storage, Antarctica ice sheet,  
 845 Greenland ice sheet, and glaciers. The sea level budget can be obtained by comparing  
 846 altimetry-based GMSL with the barystatic sea level observed by GRACE and the steric sea  
 847 level. It is evident that the sea level budget can be closed between 2002 and 2015 with  $\pm 5$   
 848 mm residual errors (Fig. 18b). However, after  $\sim 2015$ , the sum of steric and barystatic sea  
 849 level is smaller than the total sea level rise for all ocean temperature products. Previous



850 studies have attributed this misclosure to salinity data biases (Barnoud et al., 2021),  
851 altimetry data errors (Barnoud et al., 2023), and GRACE data errors (Wang et al., 2021).  
852 The steric sea level inferred from IAPv4 showed lower residual (~5 mm) between 2005–  
853 2023 than ISH and EN4 data (10~20 mm), indicating that the temperature data might be  
854 partly responsible for lack of closure of sea level budget since ~2015.  
855



856  
857 **Figure 18: (a) The sea level budget from 1960 to 2021.** Observed global mean sea level  
858 for 1960–2021 and the individual contributions from land water storage, Antarctica,





859 Greenland and Glaciers (Frederikse et al., 2020). The budget is relative to a 1959~1961  
860 baseline. Here, the Antarctica, Greenland, and Glaciers data are through 2018, and a linear  
861 extrapolation is made for 2019–2021. Land water storage is estimated by GRACE after  
862 2018. Altimetry sea level is shown in yellow dashed line for comparison. (b) Sea level  
863 budget residual time series since 2005. The residual of GMSL minus barystatic and steric  
864 sea level. The seasonal cycle is reduced based on 2005–2015 climatology. A 6-month  
865 lowpass filter is applied to reduce the noise.

866

#### 867 **4. Data availability**

868 IAPv4 global ocean temperature product is available at  
869 <http://dx.doi.org/10.12157/IOCAS.20240117.002> (Cheng et al., 2024a) and  
870 <http://www.ocean.iap.ac.cn/>.

871 IAPv4 global ocean heat content product is available at  
872 <http://dx.doi.org/10.12157/IOCAS.20240117.001> (Cheng et al., 2024b) and  
873 <http://www.ocean.iap.ac.cn/>.

874 The code used in this paper includes data quality control, and the resultant dataset is  
875 available at <http://www.ocean.iap.ac.cn/>.

876

877 The data used in this study (but not generated by this work) are listed below. IAP data are  
878 available at <http://www.ocean.iap.ac.cn/>. The NCEI/NOAA data are available at  
879 (<https://www.ncei.noaa.gov/products/climate-data-records/global-ocean-heat-content>). ISH  
880 data from (<https://climate.mri-jma.go.jp/pub/ocean/ts/v7.2/>). The EN4 data  
881 (<https://www.metoffice.gov.uk/hadobs/en4/index.html>) For SST: ERSSTv5  
882 (<https://www1.ncdc.noaa.gov/pub/data/cmb/ersst/v5/netcdf/>); COBE2  
883 (<https://psl.noaa.gov/data/gridded/data.cobe2.html>); and HadSST3  
884 (<https://www.metoffice.gov.uk/hadobs/hadsst3/data/download.html>). For sea level data:  
885 AVISO+ GMSL ([https://www.aviso.altimetry.fr/en/data/products/ocean-indicators-  
886 products/mean-sea-level.html#c15723](https://www.aviso.altimetry.fr/en/data/products/ocean-indicators-products/mean-sea-level.html#c15723)), CSR GRACE  
887 (<https://www2.csr.utexas.edu/grace/>), the data in Frederikse et al., (2020) from  
888 (<https://zenodo.org/records/3862995>). The data in von Schuckmann et al., (2023)  
889 ([https://www.wdc-climate.de/ui/entry?acronym=GCOS\\_EHI\\_1960-2020](https://www.wdc-climate.de/ui/entry?acronym=GCOS_EHI_1960-2020)). Argo data were  
890 collected and made freely available by the International Argo Program and the national  
891 programs that contribute to it (<https://argo.ucsd.edu>, <https://www.ocean-ops.org>). DEEP-C



892 data from <https://doi.org/10.17864/1947.000347>; CERES data ([https://ceres-](https://ceres-tool.larc.nasa.gov/ord-tool/jsp/EBAFTOA41Selection.jsp)  
893 [tool.larc.nasa.gov/ord-tool/jsp/EBAFTOA41Selection.jsp](https://ceres-tool.larc.nasa.gov/ord-tool/jsp/EBAFTOA41Selection.jsp)); PIOMAS ice volume data from  
894 (<http://psc.apl.uw.edu/research/projects/arctic-sea-ice-volumeanomaly/>). SCRIPPS data  
895 from ([http://sio-argo.ucsd.edu/RG\\_Climatology.html](http://sio-argo.ucsd.edu/RG_Climatology.html)); BOA data from  
896 (<https://argo.ucsd.edu/data/argo-data-products/>).

897

## 898 **5. Summary and Discussion**

899 This paper introduced a new version of the ocean temperature and heat content  
900 gridded products and described the data source and data processing techniques in detail.  
901 The key technical advances include the new QC, new or updated XBT/MBT/Bottle/APB  
902 bias corrections, new ocean temperature climatology, improved mapping approach, and  
903 grid-cell ocean volume corrections. These data and technical advances allow a better  
904 estimate of long-term ocean temperature and heat content changes since the mid-1950s  
905 from the sea surface down to 2000 m. We show that the new data product could better  
906 close the sea level and energy budgets than IAPv3. For rates of change, compared with  
907 CERES, the IAPv4 also shows a better correlation from 2005 to 2023 than IAPv3.

908 Despite several marked improvements, issues needing further investigation remain.  
909 Although inter-annual and decadal-scale changes of satellite-based EEI and observational  
910 OHC are generally consistent, a mismatch remains between EEI and OHC for their month-  
911 to-month variation, as the monthly variation of OHC is still much larger than implied by  
912 EEI. There are several possibilities, in our opinion: first, there is substantial heat storage  
913 and release for land and ice monthly, which needs to be accurately quantified; second, the  
914 accuracy of OHC estimate on a monthly basis still needs to be improved for month-to-  
915 month variation because of the limited data coverage; third, the EEI observed by CERES  
916 also suffers from sampling biases on a monthly basis. Thus, a better understanding of the  
917 monthly variation of OHC and EEI is still a research priority. Besides, the failure to close  
918 the 2015-2023 sea level budget indicates that the underlying data still has bias problems,  
919 which need to be explored and resolved.

920 Second, the application of CODC-QC in IAPv4 leads to a stronger ocean warming  
921 rate in the past decade than WOD-QC used in IAPv3 because WOD-QC removes more  
922 positive temperature anomalies than CODC-QC. This could imply that the rate of increase  
923 in OHC is still slightly underestimated and deserves an in-depth investigation. Several  
924 fundamental questions must be answered: first, are there still real temperature extremes



925 being removed by CODC-QC, such as in small warm eddies? Are the extremes well  
926 sampled by the current observation system? If not, what is the impact? Moreover, it is clear  
927 that the high latitudes where sea ice occurs are not well sampled and need more attention.

928 Third, during the development of the data product, we discovered that much metadata  
929 relating to the profiles in the World Ocean Database is missing and that much existing  
930 metadata is incorrect, also giving rise to duplicate profiles, putting a strain on the overall  
931 quality of a database of oceanic observations. More than ever, long-term concerted efforts  
932 are needed to eliminate duplicate profiles and identify and correct missing metadata using  
933 statistical methods, expert control, or machine learning techniques. For example, the  
934 International Quality-Controlled Database (iQuOD) group is coordinating some activities  
935 related to data processing techniques, uncertainty quantification, and improving the overall  
936 quality of ocean data (Cowley et al., 2021).

937 Furthermore, the quantification of uncertainty for *in situ* measurements, gridded T/OC  
938 values, and the global OHC estimates need to be improved. IAPv4 only accounts for the  
939 instrumental error and sampling/mapping error. In the future, comprehensive quantification  
940 of other uncertainty sources will be made, including the choice of climatology, vertical  
941 interpolation, XBT/MBT/APB/Bottle corrections, etc. It is also necessary to analyze the  
942 correlation between these error sources. This also helps to understand regions with larger  
943 uncertainty for OHC estimates, which supports the design of the global ocean observing  
944 system.

945

946 **Author contributions.** L.C. has worked on this study's conceptualization, coordination,  
947 methodologies, and writing the manuscript. Z.T. worked on *in situ* observation collections,  
948 metadata format, and the automated quality control procedure (CODC-QC) development.  
949 Y.P. has worked on calculating and comparing the OHC annual cycle, the mixed layer  
950 depth, and the MHT among different data sets. V.G. worked on bias correction schemes for  
951 MBT, APB, and bottle data and on developing the automated quality control procedure.  
952 H.Y. worked on the analysis of inter-annual variability. J.D. has worked on OHC trend  
953 calculation and analysis. G.L. worked on SST calculation and its analysis. H. Z. worked on  
954 global energy and sea level budget calculations and analyses. Y.L. and Y.J. worked on the  
955 volume correction. All authors have contributed to formal analysis, data validation, and  
956 editing of the original draft.

957



958 **Acknowledgement and Funding.** The IAP/CAS analysis is supported by the National  
959 Natural Science Foundation of China (Grant no. 42122046, 42076202, 42206208,  
960 42261134536), Strategic Priority Research Program of the Chinese Academy of Sciences  
961 (Grant no. XDB42040402), the new Cornerstone Science Foundation through the  
962 XPLOER PRIZE, DAMO Academy Young Fellow, Youth Innovation Promotion  
963 Association, Chinese Academy of Sciences, National Key Scientific and Technological  
964 Infrastructure project “Earth System Science Numerical Simulator Facility” (EarthLab),  
965 the Young Talent Support Project of Guangzhou Association for Science and Technology.  
966 The calculations in this study were carried out on the ORISE Supercomputer. Some data  
967 were collected onboard of R/V Shiyan 6 implementing the Open Research Cruise  
968 NORC2022-10+NORC2022-303 supported by NSFC Shiptime Sharing Projects  
969 42149910. NCAR is sponsored by the US National Science Foundation. We acknowledge  
970 the World Climate Research Programme’s Working Group on Coupled Modelling, which  
971 is responsible for CMIP, and we thank the climate modeling groups for producing and  
972 making their model output available through the Earth System Grid Federation. The Argo  
973 Program is part of the Global Ocean Observing System.

974

975 **Competing interests.** The contact author has declared that none of the authors has any  
976 competing interests.

977

## 978 **References**

- 979 Abraham, J. P., Cheng, L., Mann, M. E., Trenberth, K., and von Schuckmann, K.: The  
980 ocean response to climate change guides both adaptation and mitigation efforts.  
981 Atmospheric and Oceanic Science Letters, 15, 100221,  
982 <https://doi.org/10.1016/j.aosl.2022.100221>, 2022.
- 983 Abraham, J. P., and Cheng, L.: Intersection of Climate Change, Energy, and Adaptation.  
984 Energies. 15(16), 5886; <https://doi.org/10.3390/en15165886>, 2022.
- 985 Abraham, J. P., Baringer, M., Bindoff, N. L., Boyer, T., Cheng, L. J., Church, J. A.,  
986 Conroy, J. L., Domingues, C. M., Fasullo, J. T., Gilson, J., Goni, G., Good, S. A.,  
987 Gorman, J. M., Gouretski, V., Ishii, M., Johnson, G. C., Kizu, S., Lyman, J. M.,  
988 Macdonald, A. M., Minkowycz, W. J., Moffitt, S. E., Palmer, M. D., Piola, A. R.,  
989 Reseghetti, F., Schuckmann, K., Trenberth, K. E., Velicogna, I., and Willis, J. K.: A



- 990 review of global ocean temperature observations: Implications for ocean heat content  
991 estimates and climate change, *Rev. Geophys.*, 51, 450–483,  
992 <https://doi.org/10.1002/rog.20022>, 2013.
- 993 Argo: Argo float data and metadata from Global Data Assembly Centre (Argo GDAC).  
994 SEANOE, 2000.
- 995 Bagnell, A., and DeVries, T.: 20(th) century cooling of the deep ocean contributed to  
996 delayed acceleration of Earth's energy imbalance. *Nat. Comm.*, 12, 4604,  
997 <https://doi.org/10.1038/s41467-021-24472-3>, 2021.
- 998 Barker, P. M., and McDougall, T. J.: Two Interpolation Methods Using Multiply-Rotated  
999 Piecewise Cubic Hermite Interpolating Polynomials. *J. Atmos. Ocean Technol.*, 37,  
1000 605–619, <https://doi.org/10.1175/JTECH-D-19-0211.1>, 2020.
- 1001 Barnoud, A., Pfeffer, J., Cazenave, A., Fraudeau, R., Rousseau, V., and Ablain, M.:  
1002 Revisiting the global mean ocean mass budget over 2005–2020. *Ocean Science*, 19,  
1003 321–334, <https://doi.org/10.5194/os-19-321-2023>, 2023.
- 1004 Barnoud, A., Pfeffer, J., Guérou, A., Frery, M.-L., Siméon, M., Cazenave, A., Chen, J.,  
1005 Llovel, W., Thierry, V., Legeais, J.-F., and Ablain, M.: Contributions of Altimetry  
1006 and Argo to Non-Closure of the Global Mean Sea Level Budget Since 2016.  
1007 *Geophys Res Lett*, 48, e2021GL092824, <https://doi.org/10.1029/2021GL092824>,  
1008 2021.
- 1009 Bindoff, N. L., Cheung, W. W. L., Kairo, J. G., Arístegui, J., Guinder, V. A., Hallberg, R.,  
1010 Hilmi, N., Jiao, N., and Karim, M. S.: Changing Ocean, Marine Ecosystems, and  
1011 Dependent Communities. In *IPCC Special Report on the Ocean and Cryosphere in a  
1012 Changing Climate* [H.-O. Pörtner, D.C. Roberts, V. Masson-Delmotte, P. Zhai, M.  
1013 Tignor, E. Poloczanska, K. Mintenbeck, A. Alegría, M. Nicolai, A. Okem, J. Petzold,  
1014 B. Rama, N.M. Weyer (eds.)], Cambridge University Press, Cambridge, UK and  
1015 New York, NY, USA, pp. 447–587. <https://doi.org/10.1017/9781009157964.007>,  
1016 2019.
- 1017 Boyer, T., Domingues, C. M., Good, S. A., Johnson, G. C., Lyman, J. M., Ishii, M.,  
1018 Gouretski, V., Willis, J. K., Antonov, J., Wijffels, S., Church, J. A., Cowley, R., and  
1019 Bindoff, N. L.: Sensitivity of Global Upper Ocean Heat Content Estimates to  
1020 Mapping Methods, XBT Bias Corrections, and Baseline Climatologies, *J. Climate*,  
1021 29, 4817–4842, <https://doi.org/10.1175/JCLI-D-15-0801.1>, 2016.



- 1022 Caesar, L., Rahmstorf, S., Robinson, A., Feulner, G., and Saba, V.: Observed fingerprint of  
1023 a weakening Atlantic Ocean overturning circulation. *Nature*, 556, 191-196,  
1024 <https://doi.org/10.1038/s41586-018-0006-5>, 2018.
- 1025 Cane, M. A., and Zebiak, S. E.: A theory for El Niño and the southern oscillation. *Science*,  
1026 228, 1085-1087, <https://doi.org/10.1126/science.228.4703.1085>, 1985.
- 1027 Cheng, L.: Sensitivity of Ocean Heat Content to Various Instrumental Platforms in Global  
1028 Ocean Observing System. *Ocean-Land-Atmosphere Research*, 0,  
1029 <https://doi.org/10.34133/olar.0037>, 2024a.
- 1030 Cheng, L., and Zhu, J.: Uncertainties of the Ocean Heat Content Estimation Induced by  
1031 Insufficient Vertical Resolution of Historical Ocean Subsurface Observations. *J.*  
1032 *Atmos. Ocean Technol.*, 31, 1383-1396, [https://doi.org/10.1175/JTECH-D-13-](https://doi.org/10.1175/JTECH-D-13-00220.1)  
1033 [00220.1](https://doi.org/10.1175/JTECH-D-13-00220.1), 2014.
- 1034 Cheng, L., and Zhu, J.: Influences of the Choice of Climatology on Ocean Heat Content  
1035 Estimation. *J. Atmos. Ocean Technol.*, 32, 388-394, [https://doi.org/10.1175/JTECH-](https://doi.org/10.1175/JTECH-D-14-00169.1)  
1036 [D-14-00169.1](https://doi.org/10.1175/JTECH-D-14-00169.1), 2015.
- 1037 Cheng, L., and Zhu, J.: Benefits of CMIP5 Multimodel Ensemble in Reconstructing  
1038 Historical Ocean Subsurface Temperature Variations. *J. Climate*, 29, 5393-5416,  
1039 <https://doi.org/10.1175/JCLI-D-15-0730.1>, 2016.
- 1040 Cheng, L., Zhu, J., Cowley, R., Boyer, T., and Wijffels, S.: Time, Probe Type, and  
1041 Temperature Variable Bias Corrections to Historical Expendable Bathythermograph  
1042 Observations. *J. Atmos. Ocean. Technol.*, 31, 1793-1825,  
1043 <https://doi.org/10.1175/jtech-d-13-00197.1>, 2014.
- 1044 Cheng, L., Abraham, J., Goni, G., Boyer, T., Wijffels, S., Cowley, R., Gouretski, V.,  
1045 Reseghetti, F., Kizu, S., Dong, S., Bringas, F., Goes, M., Houpert, L., Sprintall, J.,  
1046 and Zhu, J.: XBT Science: Assessment of Instrumental Biases and Errors. *B. Am.*  
1047 *Meteorol. Soc.*, 97, 924–933, <https://doi.org/10.1175/BAMS-D-15-00031.1>, 2016.
- 1048 Cheng, L., Trenberth, K. E., Fasullo, J., Boyer, T., Abraham, J., and Zhu, J.: Improved  
1049 estimates of ocean heat content from 1960 to 2015. *Sci. Adv.*, 3, e1601545,  
1050 <https://doi.org/10.1126/sciadv.1601545>, 2017.
- 1051 Cheng, L., Trenberth, K. E., Fasullo, J. T., Mayer, M., Balmaseda, M., and Zhu, J.:  
1052 Evolution of Ocean Heat Content Related to ENSO. *J. Climate*, 32, 3529-3556,  
1053 <https://doi.org/10.1175/jcli-d-18-0607.1>, 2019.
- 1054 Cheng, L., Trenberth, K. E., Gruber, N., Abraham, J. P., Fasullo, J. T., Li, G., Mann, M. E.,  
1055 Zhao, X., and Zhu, J.: Improved Estimates of Changes in Upper Ocean Salinity and



- 1056 the Hydrological Cycle. *J. Climate*, 33, 10357-10381, <https://doi.org/10.1175/JCLI->  
1057 D-20-0366.1, 2020.
- 1058 Cheng, L., von Schuckmann, K., Abraham, J. P., Trenberth, K. E., Mann, M. E., Zanna, L.,  
1059 England, M. H., Zika, J. D., Fasullo, J. T., Yu, Y., Pan, Y., Zhu, J., Newsom, E. R.,  
1060 Bronselaer, B., and Lin, X.: Past and future ocean warming. *Nat. Rev. Earth Env.*, 3,  
1061 776-794, <https://doi.org/10.1038/s43017-022-00345-1>, 2022a.
- 1062 Cheng, L., Foster, G., Hausfather, Z., Trenberth, K. E., and Abraham, J.: Improved  
1063 quantification of the rate of ocean warming. *J. Climate*, 35, 4827–4840,  
1064 <https://doi.org/10.1175/jcli-d-20-0366.1>, 2022b.
- 1065 Cheng, L., Tan, Z., Pan, Y., Zheng, H., Zhu, Y., Wei, W., Du, J., Li, G., Ye, H., Gourteski,  
1066 V.: IAP temperature 1° gridded analysis product (IAPv4),  
1067 <http://dx.doi.org/10.12157/IOCAS.20240117.002>, 2024a.
- 1068 Cheng, L., Tan, Z., Pan, Y., Zheng, H., Zhu, Y., Wei, W., Du, J., Li, G., Ye, H., Gourteski,  
1069 V.: IAP global ocean heat content 1° gridded analysis product (IAPv4),  
1070 <http://dx.doi.org/10.12157/IOCAS.20240117.001>, 2024b.
- 1071 Chu, P. C., and Fan, C.: Global climatological data of ocean thermohaline parameters  
1072 derived from WOA18. *Scientific Data*, 10, 408, <https://doi.org/10.1038/s41597-023->  
1073 02308-7, 2023.
- 1074 Comiso, J. C., Meier, W. N., and Gersten, R.: Variability and trends in the Arctic Sea ice  
1075 cover: Results from different techniques. *J. Geophys. Res.- Oceans*, 122, 6883-6900,  
1076 <https://doi.org/10.1002/2017JC012768>, 2017.
- 1077 Cowley, R., Killick, R. E., Boyer, T., Gouretski, V., Reseghetti, F., Kizu, S., Palmer, M.  
1078 D., Cheng, L., Storto, A., Le Menn, M., Simoncelli, S., Macdonald, A. M., &  
1079 Domingues, C. M.: International Quality-Controlled Ocean Database (iQuOD) v0.1:  
1080 The Temperature Uncertainty Specification. *Front. Mar. Sci.*, 8,  
1081 <https://doi.org/10.3389/fmars.2021.689695>, 2021.
- 1082 Dangendorf, S., Frederikse, T., Chafik, L., Klinck, J. M., Ezer, T., and Hamlington, B. D.:  
1083 Data-driven reconstruction reveals large-scale ocean circulation control on coastal  
1084 sea level. *Nat. Clim. Change*, 11, 514-520, <https://doi.org/10.1038/s41558-021->  
1085 01046-1, 2021.
- 1086 de Boyer Montégut, C., Madec, G., Fischer, A. S., Lazar, A., and Iudicone, D.: Mixed  
1087 layer depth over the global ocean: An examination of profile data and a profile-based  
1088 climatology. *J. Geophys. Res.- Oceans*, 109, <https://doi.org/10.1029/2004JC002378>,  
1089 2004.



- 1090 England, M. H., McGregor, S., Spence, P., Meehl, G. A., Timmermann, A., Cai, W.,  
1091 Gupta, A. S., McPhaden, M. J., Purich, A., & Santoso, A.: Recent intensification of  
1092 wind-driven circulation in the Pacific and the ongoing warming hiatus. *Nat. Clim.*  
1093 *Change*, 4, 222-227, <https://doi.org/10.1038/nclimate2106>, 2014.
- 1094 Fasullo, J. T., and Nerem, R. S.: Altimeter-era emergence of the patterns of forced sea-  
1095 level rise in climate models and implications for the future. *P. Natl. Acad. Sci.*, 115,  
1096 12944-12949, <https://doi.org/10.1073/pnas.1813233115>, 2018.
- 1097 Frederikse, T., Landerer, F., Caron, L., Adhikari, S., Parkes, D., Humphrey, V. W.,  
1098 Dangendorf, S., Hogarth, P., Zanna, L., Cheng, L., and Wu, Y.-H.: The causes of sea  
1099 level rise since 1900. *Nature*, 584, 393-397, [https://doi.org/10.1038/s41586-020-](https://doi.org/10.1038/s41586-020-2591-3)  
1100 [2591-3](https://doi.org/10.1038/s41586-020-2591-3), 2020.
- 1101 Garcia, H. E., Boyer, T. P., Locarnini, R. A., Baranova, O. K., and Zweng, M. M.: World  
1102 Ocean Database 2018: User's Manual., T. E. A.V. Mishonov, NOAA, Silver Spring,  
1103 MD., Ed. , 2018
- 1104 Goni, G. J., Sprintall, J., Bringas, F., Cheng, L., Cirano, M., Dong, S., Domingues, R.,  
1105 Goes, M., Lopez, H., Morrow, R., Rivero, U., Rossby, T., Todd, R. E., Trinanés, J.,  
1106 Zilberman, N., Baringer, M., Boyer, T., Cowley, R., Domingues, Hutchinson, K.,  
1107 Kramp, M., Mata, M. M., Reseghetti, F., Sun, C., Bhaskar Tvs U., Volkov, D.: More  
1108 Than 50 Years of Successful Continuous Temperature Section Measurements by the  
1109 Global Expendable Bathythermograph Network, Its Integrability, Societal Benefits,  
1110 and Future. *Fron. Mar. Sci.*, 6, <http://dx.doi.org/10.3389/fmars.2019.00452>, 2019.
- 1111 Good, S. A., Martin, M. J., and Rayner, N. A.: EN4: Quality controlled ocean temperature  
1112 and salinity profiles and monthly objective analyses with uncertainty estimates. *J.*  
1113 *Geophys. Res. Oceans*, 118, 6704-6716, <https://doi.org/10.1002/2013jc009067>, 2013.
- 1114 Gouretski, V., and Koltermann, K. P.: How much is the ocean really warming? *Geophys.*  
1115 *Res. Lett.*, 34, L01610, <https://doi.org/10.1029/2006GL027834>, 2007.
- 1116 Gouretski, V. and Reseghetti, F.: On depth and temperature biases in bathythermograph  
1117 data: Development of a new correction scheme based on analysis of a global ocean  
1118 database, *Deep Sea Res.*, 57, 6, 812-833, <https://doi.org/10.1016/j.dsr.2010.03.011>,  
1119 2010.
- 1120 Gouretski, V., and Cheng, L.: Correction for Systematic Errors in the Global Dataset of  
1121 Temperature Profiles from Mechanical Bathythermographs. *J. Atmos. Ocean.*  
1122 *Technol.*, 37, 841-855, <https://doi.org/10.1175/jtech-d-19-0205.1>, 2020.





- 1123 Gouretski, V., Cheng, L., and Boyer, T.: On the Consistency of the Bottle and CTD Profile  
1124 Data. *J. Atmos. Ocean Technol.*, 39, 1869-1887, <https://doi.org/10.1175/JTECH-D->  
1125 22-0004.1, 2022.
- 1126 Gouretski, V., Roquet, F., and Cheng, L.: Measurement biases in ocean temperature  
1127 profiles from marine mammal data loggers. *J. Atmos. Ocean Technol.*, submitted,  
1128 2024.
- 1129 Gouretski, V., Kennedy, J., Boyer, T., and Köhl, A.: Consistent near-surface ocean  
1130 warming since 1900 in two largely independent observing networks. *Geophys. Res.*  
1131 *Lett.*, 39, <https://doi.org/10.1029/2012GL052975>, 2012.
- 1132 Gulev, S. K., Thorne, P. W., Ahn, J., Dentener, F. J., Domingues, C. M., Gerland, S.,  
1133 Gong, D., Kaufman, D. S., Nnamchi, H. C., Quaas, J., Rivera, J. A., Sathyendranath,  
1134 S., Smith, S. L., Trewin, B., Schuckmann, K. von, and Vose, R. S.: Changing State  
1135 of the Climate System Supplementary Material, in: *Climate Change 2021: The*  
1136 *Physical Science Basis. Contribution of Working Group I to the Sixth Assessment*  
1137 *Report of the Intergovernmental Panel on Climate Change*, edited by: Masson-  
1138 Delmotte, V., Zhai, P., Pirani, A., Connors, S. L., Péan, C., Berger, S., Caud, N.,  
1139 Chen, Y., Goldfarb, L., Gomis, M. I., Huang, M., Leitzell, K., Lonnoy, E., Matthews,  
1140 J. B. R., Maycock, T. K., Waterfield, T., Yelekçi, O., Yu, R., and Zhou, B.,  
1141 Cambridge University Press, Cambridge, United Kingdom and New York, NY,  
1142 USA, 287– 422, <https://doi.org/10.1017/9781009157896.004>, 2021.
- 1143 Hakuba, M. Z., Frederikse, T., and Landerer, F. W.: Earth's Energy Imbalance From the  
1144 Ocean Perspective (2005–2019), *Geophys. Res. Lett.*, 48, e2021GL093624,  
1145 <https://doi.org/10.1029/2021GL093624>, 2021.
- 1146 Hansen, J., Sato, M., Kharecha, P., and von Schuckmann, K.: Earth's energy imbalance and  
1147 implications. *Atmos. Chem. Phys.*, 11, 13421-13449, <https://doi.org/10.5194/acp-11->  
1148 13421-2011, 2011.
- 1149 Hirahara, S., Ishii, M., and Fukuda, Y.: Centennial-Scale Sea Surface Temperature  
1150 Analysis and Its Uncertainty. *J. Climate*, 27, 57-75, <https://doi.org/10.1175/JCLI-D->  
1151 12-00837.1, 2014.
- 1152 Holte, J., Talley, L. D., Gilson, J., and Roemmich, D.: An Argo mixed layer climatology  
1153 and database. *Geophys. Res. Lett.*, 44, 5618-5626,  
1154 <https://doi.org/10.1002/2017GL073426>, 2017.



- 1155 Hosoda, S., Ohira, T., and Nakamura, T.: Monthly mean dataset of global oceanic  
1156 temperature and salinity derived from Argo float observations. JAMSTEC Report of  
1157 Research and Development, 8, <https://doi.org/10.5918/jamstecr.8.47>, 2008.
- 1158 Huang, B., Thorne, P. W., Banzon, V. F., Boyer, T., Chepurin, G., Lawrimore, J. H.,  
1159 Menne, M. J., Smith, T. M., Vose, R. S., and Zhang, H.-M.: Extended Reconstructed  
1160 Sea Surface Temperature, Version 5 (ERSSTv5): Upgrades, Validations, and  
1161 Intercomparisons. *J. Climate*, 30, 8179-8205, [https://doi.org/10.1175/JCLI-D-16-](https://doi.org/10.1175/JCLI-D-16-0836.1)  
1162 0836.1, 2017.
- 1163 Hugonnet, R., McNabb, R., Berthier, E., Menounos, B., Nuth, C., Girod, L., Farinotti, D.,  
1164 Huss, M., Dussaillant, I., Brun, F., and Käab, A.: Accelerated global glacier mass  
1165 loss in the early twenty-first century. *Nature*, 592, 726-731,  
1166 <https://doi.org/10.1038/s41586-021-03436-z>, 2021.
- 1167 IPCC: Annex I: Observational Products [Trewin, B. (ed.)], pp. 2061–2086 pp. , 2021
- 1168 Ishii, M., and Kimoto, M.: Reevaluation of historical ocean heat content variations with  
1169 time-varying XBT and MBT depth bias corrections. *J. Oceanogr.*, 65, 287-299,  
1170 <https://doi.org/10.1007/s10872-009-0027-7>, 2009.
- 1171 Ishii, M., Shouji, A., Sugimoto, S., and Matsumoto, T.: Objective analyses of sea-surface  
1172 temperature and marine meteorological variables for the 2<sup>0</sup>h century using ICOADS  
1173 and the Kobe Collection. *Int. J. Climatol.*, 25, 865-879,  
1174 <https://doi.org/10.1002/joc.1169>, 2005.
- 1175 Ishii, M., Y. Fukuda, S. Hirahara, S. Yasui, T. Suzuki, and K. Sato: Accuracy of Global  
1176 Upper Ocean Heat Content Estimation Expected from Present Observational Data  
1177 Sets. *Sola*, 13, 163-167, <https://doi.org/10.2151/sola.2017-030>, 2017.
- 1178 Jin, F.-F.: An Equatorial Ocean Recharge Paradigm for ENSO. Part I: Conceptual Model.  
1179 *J. Atmos. Sci.*, 54, 811-829, [https://doi.org/10.1175/1520-](https://doi.org/10.1175/1520-0469(1997)054%3C0811:AEORPF%3E2.0.CO;2)  
1180 0469(1997)054%3C0811:AEORPF%3E2.0.CO;2, 1997.
- 1181 Johns, W. E., Elipot, S., Smeed, D. A., Moat, B., King, B., Volkov, D. L., and Smith, R. H.:  
1182 Towards two decades of Atlantic Ocean mass and heat transports at 26.5° N.  
1183 *Philosophical Transactions of the Royal Society A: Mathematical, Physical and*  
1184 *Engineering Sciences*, 381, 20220188, 2023.
- 1185 Johnson, G. C., Purkey, S. G., Zilberman, N. V., and Roemmich, D.: Deep Argo Quantifies  
1186 Bottom Water Warming Rates in the Southwest Pacific Basin. *Geophys. Res. Lett.*,  
1187 46, 2662-2669, <https://doi.org/10.1098/rsta.2022.0188>, 2019.



- 1188 Katsumata, K., Purkey, S. G., Cowley, R., Sloyan, B. M., Diggs, S. C., Moore, T. S.,  
1189 Talley, L. D., and Swift, J. H.: GO-SHIP Easy Ocean: Gridded ship-based  
1190 hydrographic section of temperature, salinity, and dissolved oxygen. *Scientific Data*,  
1191 9, 103, <https://doi.org/10.1038/s41597-022-01212-w>, 2022.
- 1192 Kennedy, J.: A review of uncertainty in in situ measurements and data sets of sea surface  
1193 temperature. *Rev. Geophys.*, 52, 1-32, <https://doi.org/10.1002/2013RG000434>, 2014.
- 1194 Levitus, S., Antonov, J. I., Boyer, T. P., Locarnini, R. A., Garcia, H. E., and Mishonov, A.  
1195 V.: Global ocean heat content 1955–2008 in light of recently revealed  
1196 instrumentation problems. *Geophys. Res. Lett.*, 36,  
1197 <https://doi.org/10.1029/2008GL037155>, 2009
- 1198 Levitus, S., Antonov, J. I., Boyer, T. P., Baranova, O. K., Garcia, H. E., Locarnini, R. A.,  
1199 Mishonov, A. V., Reagan, J. R., Seidov, D., Yarosh, E. S., and Zweng, M. M.: World  
1200 ocean heat content and thermosteric sea level change (0–2000 m), 1955–2010,  
1201 *Geophys. Res. Lett.*, 39, L10603, <https://doi.org/10.1029/2012GL051106>, 2012.
- 1202 Li, G., Cheng, L., Zhu, J., Trenberth, K. E., Mann, M. E., and Abraham, J. P.: Increasing  
1203 ocean stratification over the past half-century. *Nat. Clim. Change*, 10, 1116-1123,  
1204 <https://doi.org/10.1038/s41558-020-00918-2>, 2020.
- 1205 Li, H., Xu, F., Zhou, W., Wang, D., Wright, J. S., Liu, Z., and Lin, Y.: Development of a  
1206 global gridded Argo data set with Barnes successive corrections. *J. Geophys. Res.*  
1207 *Oceans*, 122, 866-889, <https://doi.org/10.1002/2016JC012285>, 2017.
- 1208 Li, Y., Church, J. A., McDougall, T. J., and Barker, P. M.: Sensitivity of Observationally  
1209 Based Estimates of Ocean Heat Content and Thermal Expansion to Vertical  
1210 Interpolation Schemes. *Geophys. Res. Lett.*, 49, e2022GL101079,  
1211 <https://doi.org/10.1029/2022GL101079>, 2022.
- 1212 Lian, T., Wang, J., Chen, D., Liu, T. and Wang, D.: A Strong 2023/24 El Niño is Staged by  
1213 Tropical Pacific Ocean Heat Content Buildup. *Ocean-Land-Atmosphere Research*, 2,  
1214 0011, <https://doi.org/10.34133/olar.0011>, 2023.
- 1215 Liu, C., and Allan, R.: Reconstructions of the radiation fluxes at the top of atmosphere and  
1216 net surface energy flux: DEEP-C version 5.0. . a. A. University of Reading Dataset,  
1217 Ed., <https://doi.org/10.17864/1947.000347>, 2022
- 1218 Liu, C., Allan, R. P., Mayer, M., Hyder, P., Loeb, N. G., Roberts, C. D., Valdivieso, M.,  
1219 Edwards, J. M., and Vidale, P.-L.: Evaluation of satellite and reanalysis-based global  
1220 net surface energy flux and uncertainty estimates. *J. Geophys. Res.- Atmospheres*,  
1221 122, 6250-6272, <https://doi.org/10.1002/2017JD026616>, 2017.



- 1222 Liu, C., Allan, R. P., Mayer, M., Hyder, P., Desbruyères, D., Cheng, L., Xu, J., Xu, F., and  
1223 Zhang, Y.: Variability in the global energy budget and transports 1985–2017, *Clim.*  
1224 *Dynam.*, 55, 3381–3396, <https://doi.org/10.1007/s00382-020-05451-8>, 2020.
- 1225 Loeb, N. G., Johnson, G. C., Thorsen, T. J., Lyman, J. M., Rose, F. G., and Kato, S.:  
1226 Satellite and Ocean Data Reveal Marked Increase in Earth’s Heating Rate. *Geophys.*  
1227 *Res. Lett.*, 48, <https://doi.org/10.1029/2021gl093047>, 2021.
- 1228 Loeb, N. G., Thorsen, T. J., Norris, J. R., Wang, H., and Su, W.: Changes in Earth’s energy  
1229 budget during and after the “Pause” in global warming: An observational  
1230 perspective, *Climate*, 6, 62, <https://doi.org/10.3390/cli6030062>, 2018.
- 1231 Lyman, J. M., and Johnson, G. C.: Estimating Global Ocean Heat Content Changes in the  
1232 Upper 1800 m since 1950 and the Influence of Climatology Choice. *J. Climate*, 27,  
1233 1945-1957, <https://doi.org/10.1175/JCLI-D-12-00752.1>, 2014.
- 1234 Lyman, J. M., Good, S. A., Gouretski, V. V., Ishii, M., Johnson, G. C., Palmer, M. D.,  
1235 Smith, D. M., and Willis, J. K.: Robust warming of the global upper ocean. *Nature*,  
1236 465, 334-337, <https://doi.org/10.1038/nature09043>, 2010.
- 1237 Mann, M.E., Beyond the Hockey Stick: Climate Lessons from The Common Era, *Proc.*  
1238 *Natl. Acad. Sci.*, 118 (39) e2112797118, <https://doi.org/10.1073/pnas.2112797118>,  
1239 2021.
- 1240 Mayer, J., Mayer, M., and Haimberger, L.: Consistency and Homogeneity of Atmospheric  
1241 Energy, Moisture, and Mass Budgets in ERA5. *J. Climate*, 34, 3955-3974,  
1242 <https://doi.org/10.1175/JCLI-D-20-0676.1>, 2021.
- 1243 Mayer, M., Alonso Balmaseda, M., and Haimberger, L.: Unprecedented 2015/2016 Indo-  
1244 Pacific Heat Transfer Speeds Up Tropical Pacific Heat Recharge. *Geophys. Res.*  
1245 *Lett.*, 45, 3274-3284, <https://doi.org/10.1002/2018GL077106>, 2018.
- 1246 McPhaden, M. J.: A 2<sup>1st</sup> century shift in the relationship between enso sst and warm water  
1247 volume anomalies. *Geophys. Res. Lett.*, 39, 9706,  
1248 <https://doi.org/10.1029/2012GL051826>, 2012.
- 1249 McMahan, C. R., Roquet, F., Baudel, S., Belbeoch, M., Bestley, S., Blight, C., Boehme,  
1250 L., Carse, F., Costa, D. P., Fedak, M. A., Guinet, C., Harcourt, R., Heslop, E.,  
1251 Hindell, M. A., Hoenner, X., Holland, K., Holland, M., Jaime, F. R. A., Jeanniard du  
1252 Dot, T., . . . Woodward: Animal Borne Ocean Sensors – AniBOS – An Essential  
1253 Component of the Global Ocean Observing System. *Front. Mar. Sci.*, 8,  
1254 <https://doi.org/10.3389/fmars.2021.751840>, 2021.



- 1255 Meyssignac, B., Boyer, T., Zhao, Z., Hakuba, M. Z., Landerer, F. W., Stammer, D., Köhl,  
1256 A., Kato, S., L'Ecuyer, T., Ablain, M., Abraham, J. P., Blazquez, A., Cazenave, A.,  
1257 Church, J. A., Cowley, R., Cheng, L., Domingues, C. M., Giglio, D., Gouretski, V.,  
1258 Ishii, M., Johnson, G. C., Killick, R. E., Legler, D., Llovel, W., Lyman, J., Palmer,  
1259 M. D., Piotrowicz, S., Purkey, S. G., Roemmich, D., Roca, R., Savita, A.,  
1260 Schuckmann, K. von, Speich, S., Stephens, G., Wang, G., Wijffels, S. E., and  
1261 Zilberman, N.: Measuring Global Ocean Heat Content to Es- timate the Earth Energy  
1262 Imbalance, *Front. Mar. Sci.*, 6, 432, <https://doi.org/10.3389/fmars.2019.00432>, 2019.  
1263 Minière, A., von Schuckmann, K., Sallée, J.-B., and Vogt, L.: Robust acceleration of Earth  
1264 system heating observed over the past six decades. *Sci. Rep.*, 13, 22975,  
1265 <https://doi.org/10.1038/s41598-023-49353-1>, 2024
- 1266 Nerem, R. S., Beckley, B. D., Fasullo, J. T., Hamlington, B. D., Masters, D., and Mitchum,  
1267 G. T.: Climate-change–driven accelerated sea-level rise detected in the altimeter era.  
1268 *P. Natl. Acad. Sci.*, 115, 2022-2025, <https://doi.org/10.1073/pnas.1717312115>, 2018.
- 1269 O'Carroll, A. G., Armstrong, E. M., Beggs, H. M., Bouali, M., Casey, K. S., Corlett, G. K.,  
1270 Dash, P., Donlon, C. J., Gentemann, C. L., Høyer, J. L., Ignatov, A., Kabobah, K.,  
1271 Kachi, M., Kurihara, Y., Karagali, I., Maturi, E., Merchant, C. J., Marullo, S.,  
1272 Minnett, P. J., Pennybacker, M., Ramakrishnan, B., Ramsankaran, R., Santoleri, R.,  
1273 Sunder, S., Saux Picart, S., Vázquez-Cuervo, J., Wimmer, W.: Observational Needs  
1274 of Sea Surface Temperature. *Front. Mar. Sci.*, 6,  
1275 <https://doi.org/10.3389/fmars.2019.00420>, 2019.
- 1276 Purkey, S. G., and Johnson, G. C.: Warming of Global Abyssal and Deep Southern Ocean  
1277 Waters between the 1990s and 2000s: Contributions to Global Heat and Sea Level  
1278 Rise Budgets. *J. Climate*, 23, 6336-6351, <https://doi.org/10.1175/2010jcli3682.1>,  
1279 2010.
- 1280 Rahmstorf, S., Box, J., Feulner, G., Mann, M.E., Robinson, A., Rutherford, S.,  
1281 Schaffernicht, E. Exceptional 2<sup>0</sup>h-Century slowdown in Atlantic Ocean  
1282 overturning, *Nature Climate Change*, 5, 475–480, 2015.
- 1283 Rayner, N. A., Parker, D. E., Horton, E. B., Folland, C. K., Alexander, L. V., Rowell, D.  
1284 P., Kent, E. C., and Kaplan, A.: Global analyses of sea surface temperature, sea ice,  
1285 and night marine air temperature since the late nineteenth century. *J. Geophys. Res.-*  
1286 *Atmospheres*, 108, <https://doi.org/https://doi.org/10.1029/2002JD002670>, 2003.



- 1287 Reiniger, R. F., and Ross, C. K.: A method of interpolation with application to  
1288 oceanographic data. *Deep Sea Research*, 15, 185-193, [https://doi.org/10.1016/0011-](https://doi.org/10.1016/0011-7471(68)90040-5)  
1289 [7471\(68\)90040-5](https://doi.org/10.1016/0011-7471(68)90040-5), 1968.
- 1290 Roemmich, D., and Gilson, J.: The 2004–2008 mean and annual cycle of temperature,  
1291 salinity, and steric height in the global ocean from the Argo Program. *Prog.*  
1292 *Oceanogr.*, 82, 81-100, <https://doi.org/10.1016/j.pocean.2009.03.004>, 2009.
- 1293 Roemmich, D., and Gilson, J.: The global ocean imprint of ENSO. *Geophys. Res. Lett.*, 38,  
1294 <https://doi.org/10.1029/2011GL047992>, 2011.
- 1295 Roemmich, D., Alford, M. H., Claustre, H., Johnson, K., King, B., Moum, J., Oke, P.,  
1296 Owens, W. B., Pouliquen, S., Purkey, S., Scanderbeg, M., Suga, T., Wijffels, S.,  
1297 Zilberman, N., Bakker, D., Baringer, M., Belbeoch, M., Bittig, H. C., Boss, E., . . .  
1298 Yasuda, I.: On the Future of Argo: A Global, Full-Depth, Multi-Disciplinary Array.  
1299 *Front. Mar. Sci.*, 6, 2019.
- 1300 Sloyan, B. M., Wanninkhof, R., Kramp, M., Johnson, G. C., Talley, L. D., Tanhua, T.,  
1301 McDonagh, E., Cusack, C., O'Rourke, E., McGovern, E., Katsumata, K., Diggs, S.,  
1302 Hummon, J., Ishii, M., Azetsu-Scott, K., Boss, E., Ansorge, I., Perez, F. F., Mercier,  
1303 H., . . . Campos, E.: The Global Ocean Ship-Based Hydrographic Investigations  
1304 Program (GO-SHIP): A Platform for Integrated Multidisciplinary Ocean Science.  
1305 *Front. Mar. Sci.*, 6, 2019.
- 1306 Tan, Z., Zhang, B., Wu, X., Dong, M., and Cheng, L.: Quality control for ocean  
1307 observations: From present to future. *Science China Earth Sciences*, 65, 215-233,  
1308 <https://doi.org/10.1007/s11430-021-9846-7>, 2022.
- 1309 Tan, Z., Cheng, L., Gouretski, V., Zhang, B., Wang, Y., Li, F., Liu, Z., & Zhu, J.: A new  
1310 automatic quality control system for ocean profile observations and impact on ocean  
1311 warming estimate. *Deep Sea Research Part I: Oceanographic Research Papers*, 194,  
1312 103961, <https://doi.org/10.1016/j.dsr.2022.103961>, 2023.
- 1313 Trenberth, K. E.: *The Changing Flow of Energy Through the Climate System*.  
1314 Cambridge University Press., <https://doi.org/10.1017/9781108979030>, 2022.
- 1315 Trenberth, K. E., and Fasullo, J. T.: Atlantic meridional heat transports computed from  
1316 balancing Earth's energy locally. *Geophys. Res. Lett.*, 44, 1919-1927,  
1317 <https://doi.org/10.1002/2016gl072475>, 2017.
- 1318 Trenberth, K. E., Fasullo, J. T., and Kiehl, J.: Earth's Global Energy Budget *Bull. Am.*  
1319 *Meteorol. Soc.*, 90, 311-324, <https://doi.org/10.1175/2008bams2634.1>, 2009.



- 1320 Trenberth, K. E., Fasullo, J. T., Von Schuckmann, K., and Cheng, L.: Insights into Earth's  
1321 Energy Imbalance from Multiple Sources. *J. Climate*, 29, 7495-7505,  
1322 <https://doi.org/10.1175/jcli-d-16-0339.1>, 2016.
- 1323 Trenberth, K. E., Zhang, Y., Fasullo, J. T., and Cheng, L.: Observation-Based Estimates of  
1324 Global and Basin Ocean Meridional Heat Transport Time Series. *J. Climate*, 32,  
1325 4567-4583, <https://doi.org/10.1175/jcli-d-18-0872.1>, 2019.
- 1326 von Schuckmann, K., and Le Traon, P. Y.: How well can we derive Global Ocean  
1327 Indicators from Argo data? *Ocean Sci.*, 7, 783-791, [https://doi.org/10.5194/os-7-783-](https://doi.org/10.5194/os-7-783-2011)  
1328 2011, 2011.
- 1329 von Schuckmann, K., Cheng, L., Palmer, M. D., Hansen, J., Tassone, C., Aich, V.,  
1330 Adusumilli, S., Beltrami, H., Boyer, T., Cuesta-Valero, F. J., Desbruyères, D.,  
1331 Domingues, C., García-García, A., Gentine, P., Gilson, J., Gorfer, M., Haim-berger,  
1332 L., Ishii, M., Johnson, G. C., Killick, R., King, B. A., Kirchengast, G.,  
1333 Kolodziejczyk, N., Lyman, J., Marzeion, B., Mayer, M., Monier, M., Monselesan, D.  
1334 P., Purkey, S., Roemmich, D., Schweiger, A., Seneviratne, S. I., Shepherd, A., Slater,  
1335 D. A., Steiner, A. K., Straneo, F., Timmermans, M.-L., and Wijffels, S. E.: Heat  
1336 stored in the Earth system: where does the energy go?, *Earth Syst. Sci. Data*, 12,  
1337 2013–2041, <https://doi.org/10.5194/essd-12-2013-2020>, 2020.
- 1338 von Schuckmann, K., Palmer, M. D., Trenberth, K. E., Cazenave, A., Chambers, D.,  
1339 Champollion, N., Hansen, J., Josey, S. A., Loeb, N., Mathieu, P.-P., Meyssignac, B.,  
1340 and Wild, M.: An imperative to monitor Earth's energy imbalance, *Nat. Clim.*  
1341 *Change*, 6, 138–144, <https://doi.org/10.1038/nclimate2876>, 2016.
- 1342 von Schuckmann, K., Minière, A., Gues, F., Cuesta-Valero, F. J., Kirchengast, G.,  
1343 Adusumilli, S., Straneo, F., Ablain, M., Allan, R. P., Barker, P. M., Beltrami, H.,  
1344 Blazquez, A., Boyer, T., Cheng, L., Church, J., Desbruyeres, D., Dolman, H.,  
1345 Domingues, C. M., García-García, A., Giglio, D., Gilson, J. E., Gorfer, M., Haimberger,  
1346 L., Hakuba, M. Z., Hendricks, S., Hosoda, S., Johnson, G. C., Killick, R., King, B.,  
1347 Kolodziejczyk, N., Korosov, A., Krinner, G., Kuusela, M., Landerer, F. W., Langer, M.,  
1348 Lavergne, T., Lawrence, I., Li, Y., Lyman, J., Marti, F., Marzeion, B., Mayer, M.,  
1349 MacDougall, A. H., McDougall, T., Monselesan, D. P., Nitzbon, J., Otosaka, I., Peng, J.,  
1350 Purkey, S., Roemmich, D., Sato, K., Sato, K., Savita, A., Schweiger, A., Shepherd, A.,  
1351 Seneviratne, S. I., Simons, L., Slater, D. A., Slater, T., Steiner, A. K., Suga, T., Szekely,  
1352 T., Thiery, W., Timmermans, M. L., Vanderkelen, I., Wijffels, S. E., Wu, T., Zemp, M.:



- 1353 Heat stored in the Earth system 1960–2020: where does the energy go? *Earth Syst.*  
1354 *Sci. Data*, 15, 1675–1709, <https://doi.org/10.5194/essd-15-1675-2023>, 2023.
- 1355 Wang, F., Shen, Y., Chen, Q., and Sun, Y.: Reduced misclosure of global sea-level budget  
1356 with updated Tongji-Grace2018 solution. *Sci Rep-Uk*, 11, 17667,  
1357 <https://doi.org/10.1038/s41598-021-96880-w>, 2021.
- 1358 Watkins, M. M., Wiese, D. N., Yuan, D. N., Boening, C., and Landerer, F. W.: Improved  
1359 methods for observing Earth's time variable mass distribution with GRACE using  
1360 spherical cap mascons. *J. Geophys. Res.- Solid Earth*, 120, 2648–2671,  
1361 <https://doi.org/10.1002/2014JB011547>, 2015.
- 1362 Wijffels, S. E., Willis, J., Domingues, C. M., Barker, P., White, N. J., Gronell, A.,  
1363 Ridgway, K., and Church, J. A.: Changing Expendable Bathythermograph Fall Rates  
1364 and Their Impact on Estimates of Thermosteric Sea Level Rise. *J. Climate*, 21, 5657–  
1365 5672, <https://doi.org/10.1175/2008jcli2290.1>, 2008.
- 1366 WMO: State of the Global Climate 2021, WMO-No. 1290, 2022.
- 1367 Wong, A. P. S., Wijffels, S. E., Riser, S. C., et al.: Argo Data 1999–2019: Two Million  
1368 Temperature-Salinity Profiles and Subsurface Velocity Observations From a Global  
1369 Array of Profiling Floats, <https://doi.org/10.3389/fmars.2020.00700>, 2020.
- 1370 Zhang, X., Church, J. A., Platten, S. M., and Monselesan, D.: Projection of subtropical  
1371 gyre circulation and associated sea level changes in the Pacific based on CMIP3  
1372 climate models. *Clim. Dyn.*, 43, 131–144, [https://doi.org/10.1007/s00382-013-1902-](https://doi.org/10.1007/s00382-013-1902-x)  
1373 [x](https://doi.org/10.1007/s00382-013-1902-x), 2014.
- 1374